NAVSWC TR 91-718

NUMERICAL METHODS FOR EXPLOSION PLUME PREDICTIONS

BY W. G. SZYMCZAK AND A. B. WARDLAW

RESEARCH AND TECHNOLOGY DEPARTMENT

12 MARCH 1993

NAVAL SURFACE WARFARE CENTER

Dahlgren, Virginia 22448-5000 • Silver Spring, Maryland 20903-5000

NAVSWC TR 91-718

NUMERICAL METHODS FOR EXPLOSION PLUME PREDICTIONS

BY W. G. SZYMCZAK AND A. B. WARDLAW
RESEARCH AND TECHNOLOGY DEPARTMENT

12 MARCH 1993

NAVAL SURFACE WARFARE CENTER
Dahlgren, Virginia 22448-5000 • Silver Spring, Maryland 20903-5000

FOREWORD

A computational study has been conducted of the plume created by an underwater explosion. Calculations have been performed with a compressible and an incompressible method. The latter method was found to be more economical in treating the relatively long term phenomena associated with the explosion plume, which takes several seconds to form and decay. Both techniques suggest that the formation of an explosion plume can be divided into five different phases: cavity formation, cavity collapse, venting, jetting, and rebound. Unfortunately, the internal plume structure predicted by calculation cannot be verified at this time due to the absence of experimental data describing the density distribution within the plume.

This work was supported jointly by the Naval Surface Warfare Center Independent Research Fund and the Office of Naval Research Mathematical Sciences Division through Dr. Richard Lau under contract N0001492WX24138.

Approved by:

CARL W. LARSON, Head
Weapons and Technology Division

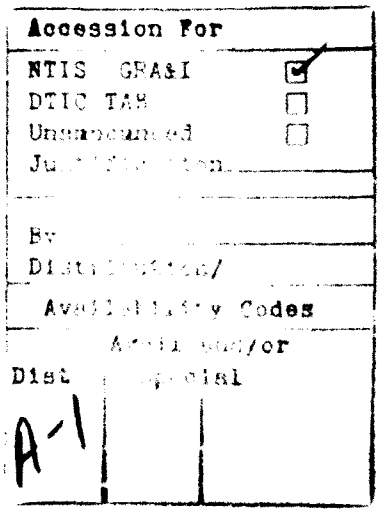

ABSTRACT

A computational study has been conducted of the plume created by an underwater explosion Calculations have been performed with a compressible and an incompressible method. The latter method was found to be more economical in treating the relatively long term phenomena associated with the explosion plume, which takes several seconds to form and decay. Both techniques suggest that the formation of an explosion plume can be divided into five different phases: cavity formation, cavity collapse, venting, jetting, and rebound. Unfortunately, the internal plume structure predicted by calculation cannot be verified at this time due to the absence of experimental data describing the density distribution within the plume.

CONTENTS

Chapter		Page
1	INTRODUCTION	1-1
2	DESCRIPTIONS OF THE NUMERICAL APPROACHES	2-1
	INCOMPRESSIBLE MODEL	2-1
	COMPRESSIBLE MODEL	2-3
3	NUMERICAL RESULTS	3-1
	INCOMPRESSIBLE RUNS	3-1
	COMPRESSIBLE RUNS	3-6
4	CONCLUSIONS	4-1
	REFERENCES	5-1
	DISTRIBUTION	(1)

ILLUSTRATIONS

Figure		Page
2-1	SLIC INTERFACE RECONSTRUCTION	2-7
3-1	COARSE GRID INCOMPRESSIBLE COMPUTATION OF A 100-POUND CHARGE OF TNT AT A DEPTH OF FIVE FEET	3-9
3-2	COARSE GRID INCOMPRESSIBLE COMPUTATION OF A 100-POUND CHARGE OF TNT AT A DEPTH OF TWELVE FEET	3-10
3-3	FINE GRID INCOMPRESSIBLE COMPUTATION OF A 100-POUND CHARGE OF TNT AT A DEPTH OF TWELVE FEET	3-11
3-4	TIME HISTORIES OF THE MAXIMUM WATER AND SPRAY HEIGHTS FOR THE TWELVE-FOOT DEPTH COMPUTATIONS	3-12
3-5	COARSE GRID INCOMPRESSIBLE COMPUTATION OF A 100-POUND CHARGE OF TNT AT A DEPTH OF SIXTEEN FEET	3-13
3-6	FINE GRID INCOMPRESSIBLE COMPUTATION OF A 100-POUND CHARGE OF TNT AT A DEPTH OF SIXTEEN FEET	3-14
3-7	TIME HISTORIES OF THE MAXIMUM COLUMN AND SPRAY HEIGHTS FOR THE SIXTEEN-FOOT DEPTH COMPUTATIONS	3-15
3-8	TIME HISTORIES OF THE MAXIMUM COLUMN HEIGHTS BASED ON THE COARSE GRID COMPUTATIONS AT CHARGE DEPTHS BETWEEN FIVE AND FOURTEEN FEET	3-16

ILLUSTRATIONS (Continued)

Figure		Page
3-9	TIME HISTORIES OF THE MAXIMUM COLUMN HEIGHTS BASED ON THE COARSE GRID COMPUTATIONS AT CHARGE DEPTHS BETWEEN FIFTEEN AND TWENTY FEET	3-17
3-10	TIME HISTORIES OF THE MAXIMUM SPRAY HEIGHTS BASED ON THE COARSE GRID COMPUTATIONS AT CHARGE DEPTHS BETWEEN FIVE AND FOURTEEN FEET	3-18
3-11	TIME HISTORIES OF THE MAXIMUM SPRAY HEIGHTS BASED ON THE COARSE GRID COMPUTATIONS AT CHARGE DEPTHS BETWEEN FIFTEEN AND TWENTY FEET	3-19
3-12	VELOCITY VECTORS FROM THE COMPRESSIBLE COMPUTATION OF A 300-POUND CHARGE OF TNT AT A DEPTH OF FIVE FEET	3-20
3-13	DENSITY CONTOURS FROM THE COMPRESSIBLE COMPUTATION OF A 300-POUND CHARGE OF TNT AT A DEPTH OF FIVE FEET	3-23
3-14	VELOCITY VECTORS FROM THE COMPRESSIBLE COMPUTATION OF A 100-POUND CHARGE OF TNT IN SHALLOW WATER AT A DEPTH OF 6.5 FEET	3-24
3-15	DENSITY CONTOURS FROM THE COMPRESSIBLE COMPUTATION OF A 100-POUND CHARGE OF TNT IN SHALLOW WATER AT A DEPTH OF 6.5 FEET	3-27

TABLES

Table		Page
3-1	SHALLOW DEPTH EXPLOSION BUBBLE INITIAL DATA	3-2
3-2	EXTRAPOLATED SHALLOW CHARGE DEPTH SPRAY HEIGHTS	3-6

CHAPTER 1

INTRODUCTION

A large body of information exists concerning plumes generated by underwater explosions. A review of much of this information can be found in References 1 through 3, which describes the general shape of the resulting plume (its height and width). However, available data does not address the issues of plume structure and the density distribution. The objective of this report is to study these questions using numerical simulation techniques. Aside from being of general scientific interest, the results from this study can be used to evaluate several defense concepts which utilize plumes generated by explosives for ship defense.[4]

As described by Cole[1] and Young,[2] the underwater explosion can be divided into two distinct phases: a compressible and an incompressible one. The compressible phase occurs early after the initiation of the explosion and is marked by the outward propagation of a shock wave from the explosion. This shock wave reflects off the water surface, leaving an upwelling of cavitated water behind which initiates the plume. The shock, which travels on the order of 1500 m/sec, leaves the domain of interest within 10 to 100 msecs. For the remainder of the problem, where the time scale is on the order of seconds, water can be effectively treated as incompressible. The dominant feature of this phase is the pulsating explosion bubble which migrates towards the free surface. This bubble starts out as a high pressure gas pocket, expanding until the pressure inside of it is less than that of the surrounding water. It then contracts and, under the influence of gravity or a surface, it loses its spherical symmetry, often forming a torus with a high velocity water jet flowing through its center. Due to these pulsations, the plume generated by the explosion bubble is sensitive to the state of the bubble as it nears the surface.

The general approach has been to model the underwater explosion phenomena using two different approaches: a compressible and an incompressible one. The compressible approach is based on the algorithm suggested by Collela, et al.[5] Here, the Euler equations are solved for both the air and water using Simple Line Interface Condition (SLIC) methodology[6] to capture the free surface. This technique should be most appropriate for the early phases of the problem. An incompressible method, described in References 7 and 8, has been employed to treat later times. This approach can efficiently and accurately predict explosion bubble dynamics, including migration and jetting.[9]

The bulk of this report concerns the incompressible calculations, which can be efficiently applied to a large number of cases. In particular, a parametric study was conducted for 100 pounds of TNT exploded at depths between 5 and 20 feet, with computations carried out at approximately

2-foot intervals. The numerical accuracy of the calculations were assessed by comparing results using different computational grids. The compressible calculations were applied to two cases: a 300-pound charge at depth of 5 feet, and a 100-pound charge in shallow water at depth of 6.5 feet.

CHAPTER 2

DESCRIPTIONS OF THE NUMERICAL APPROACHES

Two different algorithms are used to study the phenomena described in the previous section. The first algorithm is based on a model in which the water is assumed to be incompressible, while the second algorithm allows for the effects of compressibility.

INCOMPRESSIBLE MODEL

The "incompressible" model is based on a generalized formulation of hydrodynamics first proposed in Reference 10. This formulation uses a fixed spatial domain Ω, where the density ρ, velocity $\mathbf{u}$, and the pressure P are governed by the mass and momentum conservation equations

$$\rho_t + \nabla\cdot(\rho\mathbf{u}) = 0, \tag{2-1a}$$

$$(\rho\mathbf{u})_t + \nabla\cdot(\rho\mathbf{u}\mathbf{u}) = -\rho g\,\mathbf{k} - \nabla P, \tag{2-1b}$$

subject to the constraint

$$\rho \le \rho_0. \tag{2-1c}$$

where g the gravitational constant, $-\mathbf{k}$ the unit vector in the direction of the gravitational force, and ρ_0 is the constant density of the incompressible liquid. In constructing solutions for the constrained system (2-1), it is assumed that liquid-on-liquid collisions behave inelastically, thereby causing a reduction in the total mechanical energy of the flow field. These energy losses are associated with breakdowns of the classical theory and may be attributed to turbulence.[11]

The density field divides Ω into two time varying regions, namely, the *liquid region* $\mathbf{D}(t) = \{\mathbf{x} \in \Omega: \rho(\mathbf{x},t)=\rho_0\}$, and the *nonliquid region* where $\rho < \rho_0$. The interfaces separating these regions are the free surfaces. The numerical solution "captures" these surfaces as slightly smeared interfaces. The nonliquid regions are characterized by specifying uniform pressures in each of its connected subsets. For example, in the atmospheric region above the liquid the pressure is set to the ambient air pressure. In an underwater bubble the pressure P_B may be determined using the adiabatic law $P_B = CV_B^{-\gamma}$, where V_B is the instantaneous bubble volume, C is a constant, and γ is the ratio of specific heats of the bubble gases.

Assume that the density and velocity, $\rho^n, \mathbf{u}^n$ at time step n, and the pressure gradient at the previous half step, $\nabla P^{n-\frac{1}{2}}$ are known. This solution is evolved using the following three step time split procedure.

Convection

The solution is first advanced

$$(\rho^n, \mathbf{u}^n) \rightarrow (\tilde{\rho}, \tilde{\mathbf{u}})$$

by "solving" the conservation laws (2-1a,b) without including the ∇P term on the right hand side of (2-1b) and without regard to the constraint (2-1c). This step is implemented numerically using a formally second order Godunov-type method, which uses slope limiting in space and explicit predictor-corrector time stepping.

Redistribution of Density and Momenta

Next, the density and momenta are redistributed

$$(\tilde{\rho}, \tilde{\mathbf{u}}) \rightarrow (\bar{\rho}, \bar{\mathbf{u}})$$

so that the constraint (2-1c) is satisfied , the global conservation of mass and momenta are maintained, and the energy is nonincreasing. The density is redistributed using an approximate solution to an obstacle problem. This solution is obtained using a constrained direction preconditioned conjugate gradient method. The momenta redistributions are determined as solutions of two elliptic self-adjoint problems. Discretizations of these problems yield diagonally dominant matrices which are efficiently solved by a diagonally preconditioned conjugate gradient method. After this step $\bar{\rho} = \rho^{n+1}$, and the new nonliquid region is then determined along with the pressure in each of its connected subsets. In the computational space the new liquid region, $\mathbf{D}^{n+1} = \mathbf{D}(t^{n+1})$, is defined to be the collection of grid cells $C_{i,j}$ such that

$$\rho_{i,j}^{n+1} \geq (1-\varepsilon_\rho)\rho_0, \tag{2-2}$$

where $\rho_{i,j}^{n+1}$ is the density in cell $C_{i,j}$. A typical value used for ε_ρ is 0.04. At this stage $\bar{\mathbf{u}} = \mathbf{u}^{n+1}$ in the new non-liquid region. However, $\bar{\mathbf{u}}$ is not consistent with (2-1b) in the new liquid region.

Pressure Projection

In this step the velocity is corrected

$$\bar{\mathbf{u}} \rightarrow \mathbf{u}^{n+1}$$

using the gradient of the new pressure, $P^{n+\frac{1}{2}}$. The pressure $P = P^{n+\frac{1}{2}}$ is the solution of

$$\tau \Delta P = \rho_0 \nabla \cdot \bar{\mathbf{u}} \qquad in \quad \mathbf{D}^{n+1}$$

where τ is the time step. This equation is discretized using a finite element method with bilinear elements, and the resulting linear system is solved using an incomplete Cholesky preconditioned conjugate gradient method. The new velocity

$$\mathbf{u}^{n+1} = \bar{\mathbf{u}} - \frac{\tau \nabla P^{n+\frac{1}{2}}}{\rho_0}$$

is divergence free in $\mathbf{D}^{n+1}$ and thus is consistent with (2-1b).

A more complete description of the motivation and discretization of the above three steps are discussed in References 7 through 9.

COMPRESSIBLE MODEL

The compressible model uses the technique outlined in Reference 5. Here, the flow is described by the 2-D Euler Equations in cylindrical coordinates:

$$\frac{\partial Q}{\partial t} + \frac{\partial U}{\partial r} + \frac{\partial F}{\partial z} = S, \tag{2-3}$$

where

$$Q = \begin{bmatrix} \rho \\ \rho u \\ \rho v \\ \rho E \end{bmatrix}, \quad U = \begin{bmatrix} \rho u \\ \rho u^2 + p \\ \rho uv \\ \rho H \end{bmatrix},$$

$$F = \begin{bmatrix} \rho u \\ \rho uv \\ \rho v^2 + p \\ \rho H \end{bmatrix}, \quad S = \left[\frac{1}{r}\right]\begin{bmatrix} \rho u \\ \rho u^2 + p \\ \rho uv \\ \rho uH \end{bmatrix}, \tag{2-4}$$

$$E = e + .5(u^2 + v^2) \; ; \; H = h + .5(u^2 + v^2).$$

Here, e, h, u, v, p, and ρ are the energy, enthalpy, radial velocity, axial velocity, and density in single property cells. In mixed cells, these are mass averaged properties for the cell. Additional variables are also computed in mixed cells: f (volume fraction), ρ and E for each substance.

The numerical technique used to solve the above equations is based on a time splitting approach which divides the two-dimensional problem into two one-dimensional problems in the r and z directions:

$$(r \; direction) \quad \frac{\partial Q}{\partial t} + \frac{\partial U}{\partial r} = S \tag{2-5}$$

$$(z \; direction) \quad \frac{\partial Q}{\partial t} + \frac{\partial F}{\partial z} = 0. \tag{2-6}$$

The complete problem was simulated by solving the above at each step in succession.

A second order Godunov scheme is used to solve each one-dimensional problem. This method consists of a predictor and corrector step and is described in detail in Reference 12. In regions of the flow containing a single species, this method consists of the following steps:

1. Property derivatives are computed using a limited second order differencing procedure, that reduces derivative values in non-smooth regions of the flow field.

2. The predictor step is based on a method of characteristics and determines properties at the cell edges center (i.e., $x_{i,j\pm\frac{1}{2}}$, $t + \frac{\Delta t}{2}$). This produces two sets of property values at each cell edge center, one from each of the adjacent cells
3. The corrector step applies a linear Riemann problem, using these two sets of values as initial states, to determine corrected properties at the cell edge centers.
4. Corrector cell edge center properties are used to advance Q and hence the cell properties.

In multiple fluid regions, the algorithm must be modified. The first modification consists of applying the single species procedure using average properties. For an air-water mixture, the average density and energy follow from conservation:

$$\rho = f_a \rho_a + f_w \rho_w ,$$
$$E = \frac{f_a \rho_a E_a + f_w \rho_w E_w}{\rho} , \tag{2-7}$$

where

$$f_a = \frac{V_a}{V} = volume\ fraction\ of\ air ,$$

and

$$f_w = \frac{V_w}{V} = volume\ fraction\ of\ water$$

Here, the subscripts a and w refer to air and water, respectively. The average pressure is calculated by defining Γ_a and Γ_w, the inverse of which are a measure of the compressibility of air and water, respectively. For example, for substance α,

$$\Gamma_\alpha = -\left[\frac{\delta V_\alpha}{V_\alpha}\right]\left[\frac{p_\alpha}{\delta p_\alpha}\right] . \tag{2-8}$$

Noting that V is proportional to v, the specific volume, assuming an isentropic variation of v with p, and applying the definition of the speed of sound,

$$a_\alpha^2 = \left[\frac{\partial p_\alpha}{\partial \rho_\alpha}\right]_s = -v_\alpha^2\left[\frac{\partial p_\alpha}{\partial v_\alpha}\right]_s , \tag{2-9}$$

yields

$$\Gamma_\alpha = \frac{a_\alpha^2 \rho_\alpha}{p_\alpha} \tag{2-10}$$

The definition of Γ for a mixture follows by expansion:

$$\frac{1}{\Gamma} = -\left[\frac{p}{\delta p}\right]\left[\frac{\delta V}{V}\right] = -\left[\frac{p}{\delta p}\right]\left[\frac{\delta V_a + \delta V_w}{V}\right]$$

$$= -\left[\frac{p}{\delta p}\right]\left[\frac{\delta V_a}{V_a}\frac{V_a}{V} + \frac{\delta V_w}{V_w}\frac{V_w}{V}\right] = -\left[\frac{p}{\delta p}\right]\left[\frac{\delta V_a}{V_a}f_a + \frac{\delta V_w}{V_w}f_w\right] \tag{2-11}$$
$$= \frac{f_a}{\Gamma_a} + \frac{f_w}{\Gamma_w}$$

To determine the average pressure for a mixture, a change in substance volume is computed which produces the same pressure, $\hat{p}$, in each component. Defining the change in pressure of a component to be $\delta p = (p_a - \hat{p})$, enforcing conservation of volume $\delta V_a + \delta V_w = 0$, and using Equation (2-8) yields

$$\frac{V_a(p_a - \hat{p})}{\Gamma_a \hat{p}} + \frac{V_w(p_w - \hat{p})}{\Gamma_w \hat{p}} = 0,$$

(2-12)

$$\hat{p} = \Gamma\left[\frac{f_a p_a}{\Gamma_a} + \frac{f_w p_w}{\Gamma_w}\right].$$

Finally, the average speed of sound for a mixture is defined by

$$a^2 = f_a a_a^2 + f_w a_w^2. \tag{2-13}$$

The second modification of the algorithm for mixtures consists of the following steps:

1. Update the volume fraction of air and water in each cell. This is accomplished in three stages:
   a. Determine the distribution of the air and water volume fractions in each cell using SLIC algorithm. This method examines the contents of neighboring cells and sets the air-water interface to one of the options shown in Figure 2-1
   b. Use the cell edge velocity determined by the linear, average property Riemann solution to compute the volume of each substance crossing a cell edge.
   c. Update the volume fractions in each cell using the fluxes determined at stage b. The sum of the new fractions will not necessarily equal the cell volume. Adjustments are made by compressing or expanding the cells' contents assuming a relative compressibility for air and water as defined by $1/\Gamma_a$ and $1/\Gamma_w$. The resulting correction to f is

$$f_\alpha = \tilde{f}_\alpha\left[1 + \frac{\Gamma}{\Gamma_\alpha}\left(V - \tilde{V}\right)\right], \tag{2-14}$$

   where quantities with a tilde are the uncorrected values.
2. Compute the air and water mass, momentum and energy flux into each cell. This is accomplished by applying first order upwind differencing. Using the volume fractions computed in the previous step, the density and energy of each substance can be determined.
3. Determine an average cell pressure using Equation (2-12). Adjust the volume fraction of each substance to make its pressure equal to the average pressure using

$$f_\alpha^{n+1} = \tilde{f}_\alpha \left[1 + \frac{(p_\alpha - \hat{p})}{\Gamma \hat{p}} \right] \tag{2-15}$$

4. Alter ρ_α and E_α to reflect the new volume fractions.

POSSIBILITIES				INTERFACE CONSTRUCTION				
	Cell j-1	Cell j	Cell j+1		Cell j			
1.	A	M	W		A		W	
	A	M	M					
	M	M	W					
2.	W	M	W		W	A	W	
	.							
	.							
3.	W	M	A		W		A	
	W	M	M					
	M	M	A					
4.	M	M	M		A			
	.				W			
	.							
5.	A	W	A		A	W	A	
	.							
	.							

FIGURE 2-1. SLIC INTERFACE RECONSTRUCTION

CHAPTER 3

NUMERICAL RESULTS

Calculations of shallow depth underwater explosions using both the incompressible and compressible codes are presented in this chapter. Using the incompressible code a parametric study was performed on the charge depth which ranged from 5 to 20 feet. The validity of the numerical results was checked at several depths where the calculations were repeated on a computational grid with finer resolution.

INCOMPRESSIBLE RUNS

In the incompressible code, the underwater explosion bubble is modeled as a void (zero density) with a uniform pressure governed by the adiabatic gas law

$$PV^{\gamma} = constant,$$

where

P is the *bubble pressure*,
V is the *bubble volume*,

and

$\gamma = 1.3$ is the *ratio of specific heats of the bubble gases*.

Initially, the bubble is assumed to be at rest (that is, the velocity of the surrounding water is zero) and has an *initial radius* $R_0 = R_{min}$, and pressure P_0. Values for R_0 and P_0 are determined using

$$R_0 = JNW^{1/3}, \tag{3-1}$$

$$P_0 = P_{\infty}(1-\gamma)\left[\frac{1-a^3}{1-a^{3(1-\gamma)}}\right], \tag{3-2}$$

where

$J = 13.1$ is the *charge radius constant* for TNT,[13]
$N = 0.023$ is the *charge radius ratio* for TNT,
$W = 100$ is the *charge weight* in pounds,
P_{∞} is the *hydrostatic pressure* at the charge depth,

and

$$a = \frac{R_{max}}{R_{min}} \text{ is the } \textit{ratio of maximum to minimum bubble radii.}$$

The radius ratio N is an empirically determined constant such that

$$a = \frac{1}{NP_{\infty}^{1/3}}, \tag{3-3}$$

provided that P_{∞} is measured in units of feet of water (fw). In the above, R_{max} is the "free field" value for the maximum bubble radius in the case of a bubble in an infinite medium in the absence of gravity. (In this case P_{∞} denotes the ambient pressure or the pressure at infinity.) Given a value for a, and an ambient pressure P_{∞}, equation (3-2) is derived from an exact integration of the equations of motion for a spherically symmetric bubble in an infinite medium. This equation is often referred to as the Rayleigh Plesset equation.[1]

Incompressible calculations were performed simulating a one hundred pound charge of TNT at depths ranging from 5 to 20 feet. For this charge it follows from (3-1) that $R_0 = 1.39851$ feet. The ambient hydrostatic pressure is determined from

$$P_{\infty} = d + P_A \tag{3-4}$$

where

d is the *initial charge depth*,

and

$P_A = 33.9$ feet of water is the *air pressure*.

Table 3-1 lists the values of the initial bubble pressure, free field maximum bubble radius, and scaled charge depth

$$c = \frac{d}{R_{max}}$$

for the cases studied in this report.

TABLE 3-1. SHALLOW DEPTH EXPLOSION BUBBLE INITIAL DATA

d (ft)	P_0 (fw)	R_{max} (ft)	ε
5.0	27401.4	17.9	0.279
8.0	27469.6	17.5	0.457
10.0	27513.5	17.2	0.580
12.0	27555.9	17.0	0.707
14.0	27597.2	16.7	0.838
16.0	27637.5	16.5	0.969
18.0	27676.7	16.3	1.104
20.0	27714.9	16.1	1.243

Each grid used for the calculations consisted of a region of uniform cells of size $\Delta r = \Delta z = h$ in the region $r \leq 27.0$, and $-36.0 \leq z \leq 72.0$ of axisymmetric (r,z) space. For our coarse grid runs this region was divided into 39×156 cells. Cell stretching was used to extend the boundaries of the computational domain to $z = -100$, $z = 140$, and $r = 140$. The grid spacing was halved in each direction for the fine grid.

Figure 3-1 displays density contours and velocity vectors at six different times for the coarse grid run at charge depth $d = 5$ feet. In this figure, ten contours are shown, with five concentrated between zero and $0.1\rho_0$ and the remaining five between $0.1\rho_0$ and ρ_0.

In the first frame of Figure 3-1 the bubble has already vented. The contours above the cavity represent regions of "spray" where the density is below the value $(1-\varepsilon_\rho)\rho_0=0.96\rho_0$, and is treated as a nonliquid region in the code. Once the bubble "vents", (a bubble cell comes in contact with an air cell) the pressure of the cavity is given the value of the ambient air pressure instantaneously (see Reference 9 for details). Therefore, the interaction of the spray and the high pressure explosive gases with the air is not adequately described with the incompressible model.

The second frame of Figure 3-1 shows the cavity at its maximum depth of about 20 feet, just before it begins its rebound. The initial stages of the rebound is seen in the third frame (at $t \approx 1$ second) which shows the cavity refilling from the bottom up, while the outer fringes of the cavity are expanding out and falling away. At this point the velocity of the water along the centerline attains its maximum value of approximately 45 feet per second. In the fourth frame a tapered column of water has clearly formed, rising approximately 10 feet above the sea level. This column continues to move upward with a velocity of about 32 feet per second. The water column reaches its maximum height of 25 feet in the fifth frame ($t \approx 2.4$ seconds). Here, the column has a diameter of approximately 34 feet at sea level, tapering to a 22-foot diameter at a 10-foot elevation, and a 15-foot diameter at a 20-foot elevation. Finally, the sixth frame shows the column beginning to fall downward, due to the influence of gravity.

Figure 3-2 displays the computed evolution of the explosion of a charge at a depth of 12 feet. The first frame shows an early stage of the bubble expansion. The surface above the bubble has a slight bulge, and the bubble has not yet vented into the atmosphere. The contours shown inside the bubble are a numerical artifact due to remnants of cells which were initially only partially filled with water ($\rho < 0.96\rho_0$), and were treated as nonliquid cells having no pressure gradients, and therefore no velocity. The bubble vents at $t \approx 0.2$ second, but the cavity continues to increase in size, reaching its maximum depth of approximately 27 feet in the second frame ($t \approx 0.4$ second). A thin layer of relatively high density liquid (not adequately resolved on this grid) persists above the cavity, even until the third frame where the cavity rebound has commenced. Similar to the $d = 5$ case, the centerline velocity of the water attains its maximum value, of approximately 55 feet per second at this time. The water column has risen 15 feet above sea level, and is moving with a velocity of about 40 feet per second in the fourth frame ($t \approx 1.5$ seconds). The fifth frame ($t \approx 2.8$ seconds) shows the water column at its maximum height of 42 feet. This column has a base diameter of 45 feet, tapering to 20 feet at a 20-foot elevation, and approximately maintaining this diameter to the top. The bulge seen at a 30-foot elevation has a slightly lower density than water. The final frame is very similar to the previous frame, but the velocity vectors indicate that the column is beginning to fall under the influence of gravity. The remnants of the low density layer can still be seen above the column.

The $d = 12$ case was repeated on the fine grid as a numerical validity check. The fine grid results shown in Figure 3-3 reveal more detail in the "domed" region above the bubble at early times, a greater resolution of the outer thin layer surrounding the water column at later times, and a thin jet of water and spray ejected upward along the centerline axis. The water column shape, width, and height predictions are very similar for the two computations.

A more quantitative comparison between the coarse and fine grid computations of the $d = 12$ case is presented in Figure 3-4. In this figure the *column height* is defined to be the location of the lowest contour of $\rho = 0.96\rho_0$ crossing the axis, the *water height* is the highest contour of $\rho = 0.96\rho_0$, and the *spray height* is the highest contour of $\rho = 0.1\rho_0$. The column heights (which at early times represent the location of the bottom of the bubble) are in close agreement throughout the entire time interval. The discrepancies in the water heights indicate that the coarse grid has insufficient resolution for the top of the domed region above the bubble and subsequently above the water column. In the coarse grid computation no water cells remain above the water column after approximately $t = 1.4$ seconds. The jagged graphs of both the water height and spray height from the coarse grid calculation are also due to insufficient resolution of the dome region. The graph of the maximum spray height for the fine grid follows a nearly parabolic trajectory as it is decelerated by gravity, reaching a maximum height of over 80 feet.

The evolution of an explosion with an initial charge depth of 16 feet is displayed in Figure 3-5. In the second frame the bubble attains its maximum size. A significant "bump" has formed above the bubble, having an average density of approximately $0.5\rho_0$. The code treats this bump as a uniform pressure nonliquid region being decelerated by gravity. This bump is caused by the initial upward acceleration due to the high pressure bubble, followed by a deceleration once the bubble

pressure falls below the atmospheric pressure. In the third frame the water jet has passed through the bubble and is impacting a thin layer of water which was the top surface of the bubble. At this point the bubble is an annular region. The fourth frame shows the water jet rising as a column of water about twenty feet above the surface. The water column is being impeded by the relatively high density spray in the bump which is now falling downward. The interaction of the water column with the spray causes a radially outward movement of spray as depicted in the fifth frame. Here, the water column has reached its maximum height of about 40 feet, but its diameter has diminished to only 10 feet. However, a significant amount of spray, having a density of about $0.2\rho_0$ has spread out in a region having an 80-foot diameter. Finally, the sixth frame shows the column and spray falling downward due to gravity.

The d = 16 case was also repeated on the fine grid. These results are shown in Figure 3-6, which are qualitatively similar to the coarse grid results (Figure 3-5) for the first four frames, but reveal a much higher and thinner water column in the final two frames. Furthermore, this column is surrounded by a complex pattern of relatively dense layers having a maximum diameter of about 50 feet, and rising to an elevation of about 60 feet. The complexity of the flow field at the later times is due to the interactions of the primary water jet with the top surface of the bubble.

Quantitative differences between the coarse and fine grid results for the d = 16 case are shown in Figure 3-7. The almost discontinuous increases in the column heights (particularly evident for the fine grid run) are caused when the water jet impacts the top part of the bubble, which has formed a downward jet. This downward jet can be seen in the second frame of Figure 3-6. This phenomenon has also been reported experimentally by Blake and Gibson[14] and computationally using a boundary integral method by Blake, Taib and Doherty.[15] Just after the impact of the top and bottom surfaces of the bubble, the column height is abruptly changed from the height of the lower jet to the top of the water level along the axis. The relatively large discrepancies in the spray and column heights at later times suggest that further grid refinement studies should be performed due to the complex nature of this problem.

Figures 3-8 and 3-9 show the time histories of the water column heights for the coarse grid runs at depths between 5 and 14 feet, and 15 and 20 feet, respectively. The steepness of the curves in the deeper cases is once again due to the lower jet impacting the water at the top of the bubble. In the shallow cases the water at the top of the bubble has been pushed away due to the initial acceleration of the explosion. These figures indicate that a depth of 14 feet is optimal for attaining the highest water column. However, while the shallow depth cases are probably being predicted accurately (as evidenced by the small discrepancies in the coarse and fine grid runs at 12 feet), the errors in the deeper cases are greater and higher column heights than that predicted from the coarse grid runs can be expected (cf. Figure 3-7). However, it is probably safe to conclude that the optimal depth for attaining the maximum column height is between 12 and 16 feet for a 100-pound charge of TNT.

The time histories of the computed coarse grid spray heights are displayed in Figures 3-10 and 3-11. The abrupt drop in the maximum spray height values at the shallow charge depths (less than

twelve feet) are primarily numerical artifacts due to the grid stretching above 72 feet. As the spray moves upward into the larger cells, the average cell densities decrease until they fall below $0.1\rho_0$. Table 3-2 lists extrapolated spray heights obtained from the spray heights before the abrupt drop off. The extrapolation is based on the assumption that the spray is being decelerated by gravity. Since wind resistance is neglected in these extrapolations, we expect these values are larger than those which would result from actual experiments.

TABLE 3-2. EXTRAPOLATED SHALLOW CHARGE DEPTH SPRAY HEIGHTS

Charge Depth (ft)	Approximate Initial Velocity (ft	Maximum Spray Height sec)	Time of Maximum (ft)
5	300	1400	9.4
8	180	500	5.6
10	120	220	3.7
12	80	100	2.5

Experimental data for 300-pound charges of TNT has been collected by Young.[2] Since the bubble scales with the cube root of the charge weight (cf. 3-1) our results can be compared to those in Reference 2 by scaling the depth by $3^{1/3}$. Except for the extrapolated heights for the shallow cases a=5 and a=8, the results in Table 3-2 and Figures 3-10 and 3-11 greatly under estimate the maximum plume heights reported by Young.[2] However, we are unaware of publications reporting the density inside of experimentally produced plumes. It is possible that they are comprised of a very low density mix of steam and explosion gases, which are not modeled using the incompressible code.

COMPRESSIBLE RUNS

Two computations were carried out using the compressible code. The first simulated a 300 pound TNT explosion at a depth of 5 feet. Here a perfect gas equation of state was used to model the air/explosive products with $\gamma = 1.4$. This calculation was carried out in two phases:

1. A 1-D spherical calculation tracked the initial expansion of the explosion bubble to the point where the explosive shock neared the water surface.
2. A 2-D axisymmetric calculation continued the calculation to later times.

The 1-D calculation was initiated from a constant pressure bubble at rest with the following properties:

$$P_0 = 7.6742(10^{10})\ dynes/cm^2, \qquad \rho = 1.63\ gm/cm^3, \qquad R_0 = 26.84\ cm$$

The results of this computation are shown in Figures 3-12 and 3-13. Figure 3-12 illustrates the velocities in both air and water throughout the simulation. The heavy line running through these figures is the air-water interface. The complex interface geometry is more clearly visible in Figure 3-13 which provides a density contour plot. The description of the explosion provided by the simulation can be divided into four phases:

1. Bubble Venting. The bubble vents within the first 10 to 20 milliseconds.
2. Cavity formation. A deep air cavity is carved out in the water by the explosive. This cavity reaches its maximum depth at about 0.5 second.
3. Cavity collapse. Cavity venting leads to a gas pressure which is too low to sustain the cavity. Water rushes into the cavity to re-establish to original water pressure.
4. Rebound. Water rushing into the cavity impacts at the cavity center producing a plume, which in this case rises to a height of 4 meters

Absent from the above description is the interaction of the original explosion shock with the surface. In this case, the time difference between venting and the arrival of the shock is very small, and the shock does not appear to have a significant effect on the plume.

The second case considered consisted of 100 pounds of TNT exploded at a depth of 6.5 feet in water which was 13.1 feet deep. For this case, the explosive products/air were modeled by the Jones-Wilkins-Lee (JWL) equation of state, which has the form:

$$p = f_1(v) + f_2(v) + \frac{\omega e}{v} \tag{3-5}$$

$$f_\alpha = \upsilon_\alpha \left[1 + \frac{C_\alpha}{v}\right] e^{(\chi_\alpha v)}$$

For TNT the constants are defined as:

$$\begin{aligned} \upsilon_1 &= 3.760(10^{12})\ dynes/cm^2 \\ \upsilon_2 &= 3.273(10^{10})\ dynes/cm^2 \\ C_1 &= -.0443492\ cm^3/gm \\ C_2 &= -.19373\ cm^3/gm \\ \chi_1 &= -6.7645\ gm/cm^3 \\ \chi_2 &= -1.5485\ gm/cm^3 \\ \omega &= .30. \end{aligned} \tag{3-6}$$

The calculation was initiated using a one dimensional detonation model[16] which provided a non uniform pressure, velocity and density profile at the instant at which the detonation front, which was initiated at the center of the charge, reached the charge surface. The radius of the initial charge was 18.8 cm. As in the previous calculation, this case was continued using a 1 D solution until the shock was close to the surface. The calculation was then restarted using 2 D, asymmetric coordinates.

The results from the second calculation are shown in Figures 3-14 and 3-15. Figure 3-14 illustrates the velocity vectors for both air and water, with the interface shown as a solid line. Density contours are given in Figure 3-15 and clearly indicate the evolution of the water-gas interface. The explosion phases shown in Figures 3-14 and 3-15 clearly parallel those of the first case (Figures 3-12 and 3-13). The venting, cavity formation, and cavity collapse stages are all evident, however, a strong rebound is not. This may be a consequence of the large region of air-water mixture which appears along the center line. Presumably, the entrained air imparts a compressibility to the mixture which absorbs the energy of cavity collapse, thus preventing the formation of a water column.

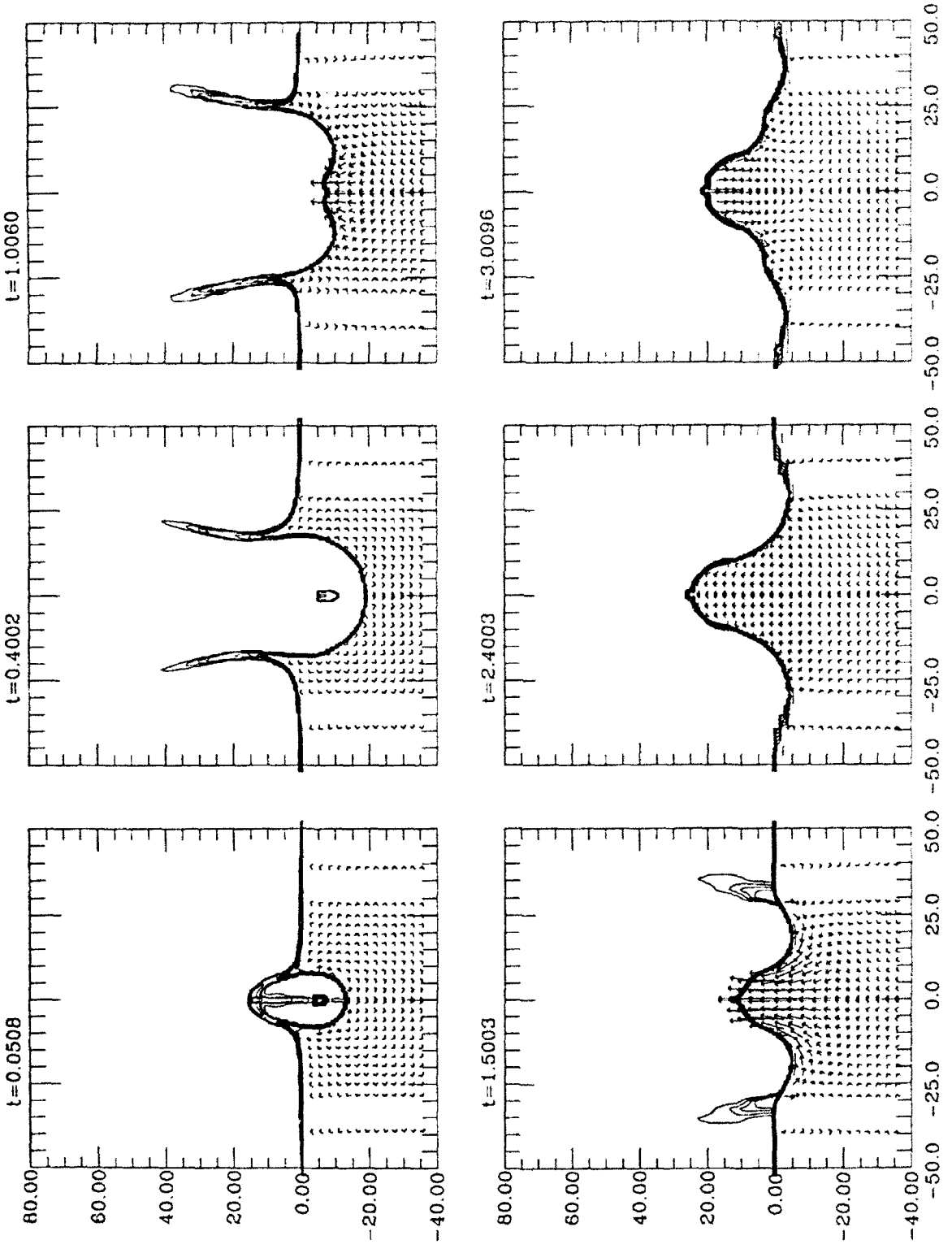

FIGURE 3-1. COARSE GRID INCOMPRESSIBLE COMPUTATION OF A 100-POUND CHARGE OF TNT AT A DEPTH OF FIVE FEET

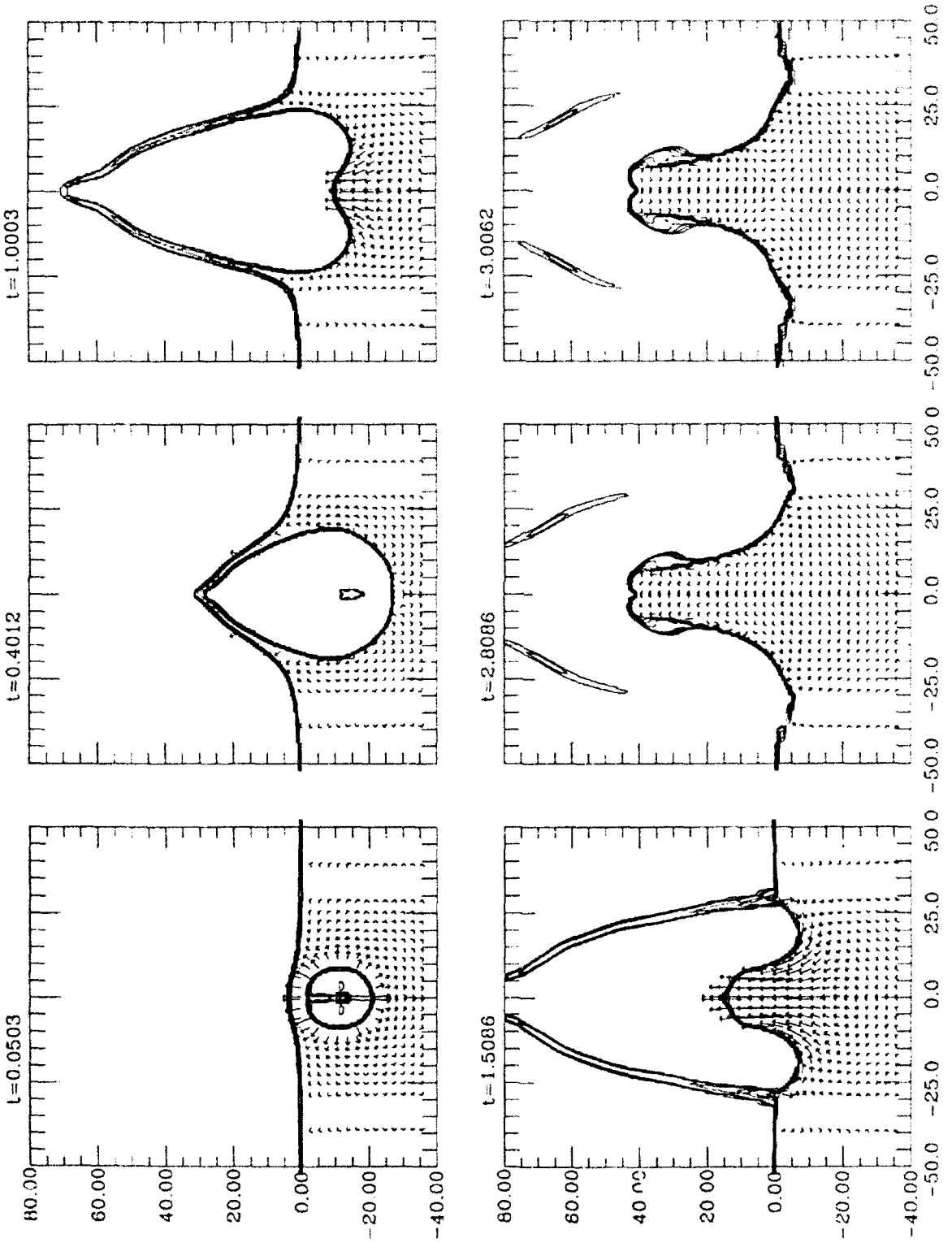

FIGURE 3-2. COARSE GRID INCOMPRESSIBLE COMPUTATION OF A 100-POUND CHARGE OF TNT AT A DEPTH OF TWELVE FEET

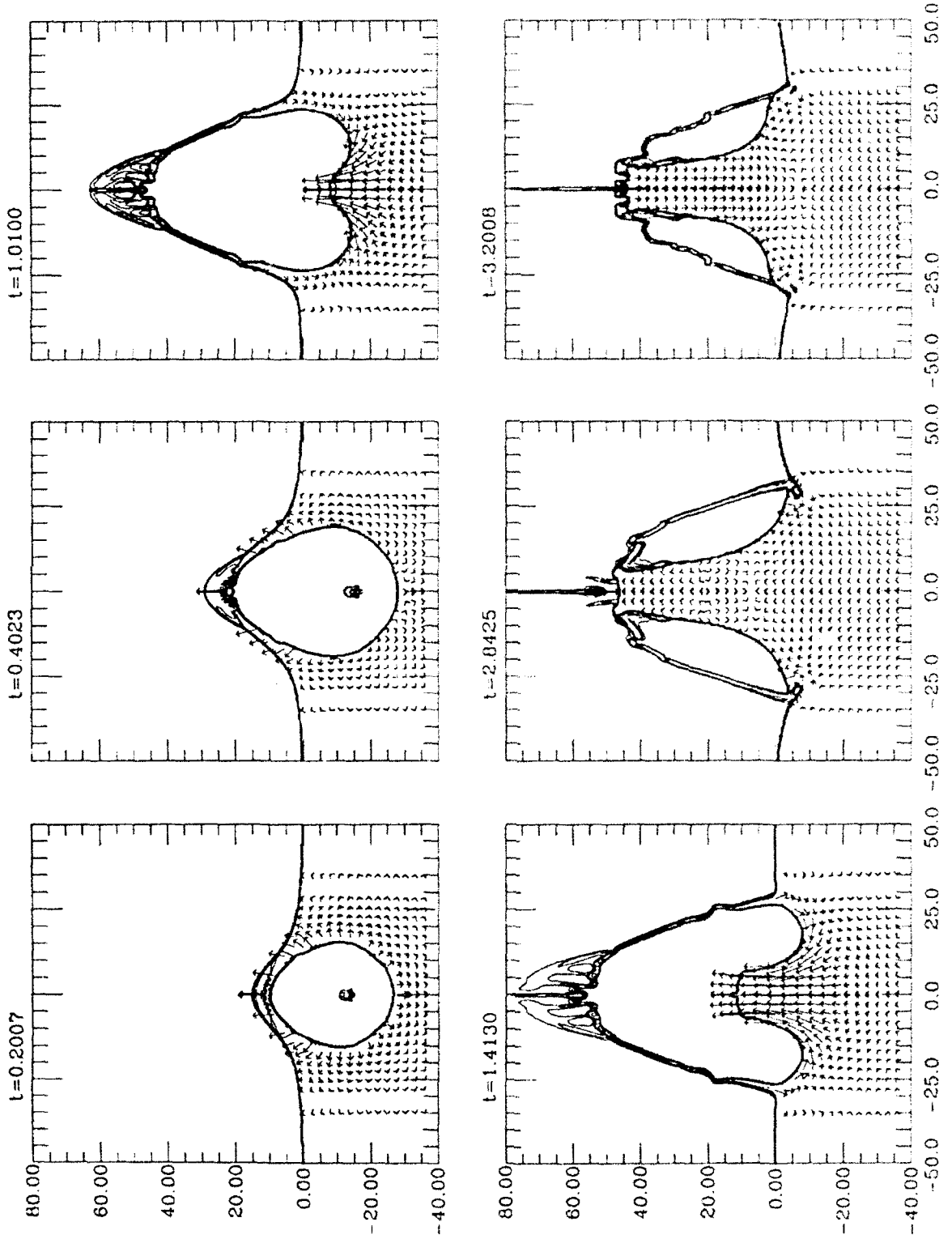

FIGURE 3-3. FINE GRID INCOMPRESSIBLE COMPUTATION OF A 100-POUND CHARGE OF TNT AT A DEPTH OF TWELVE FEET

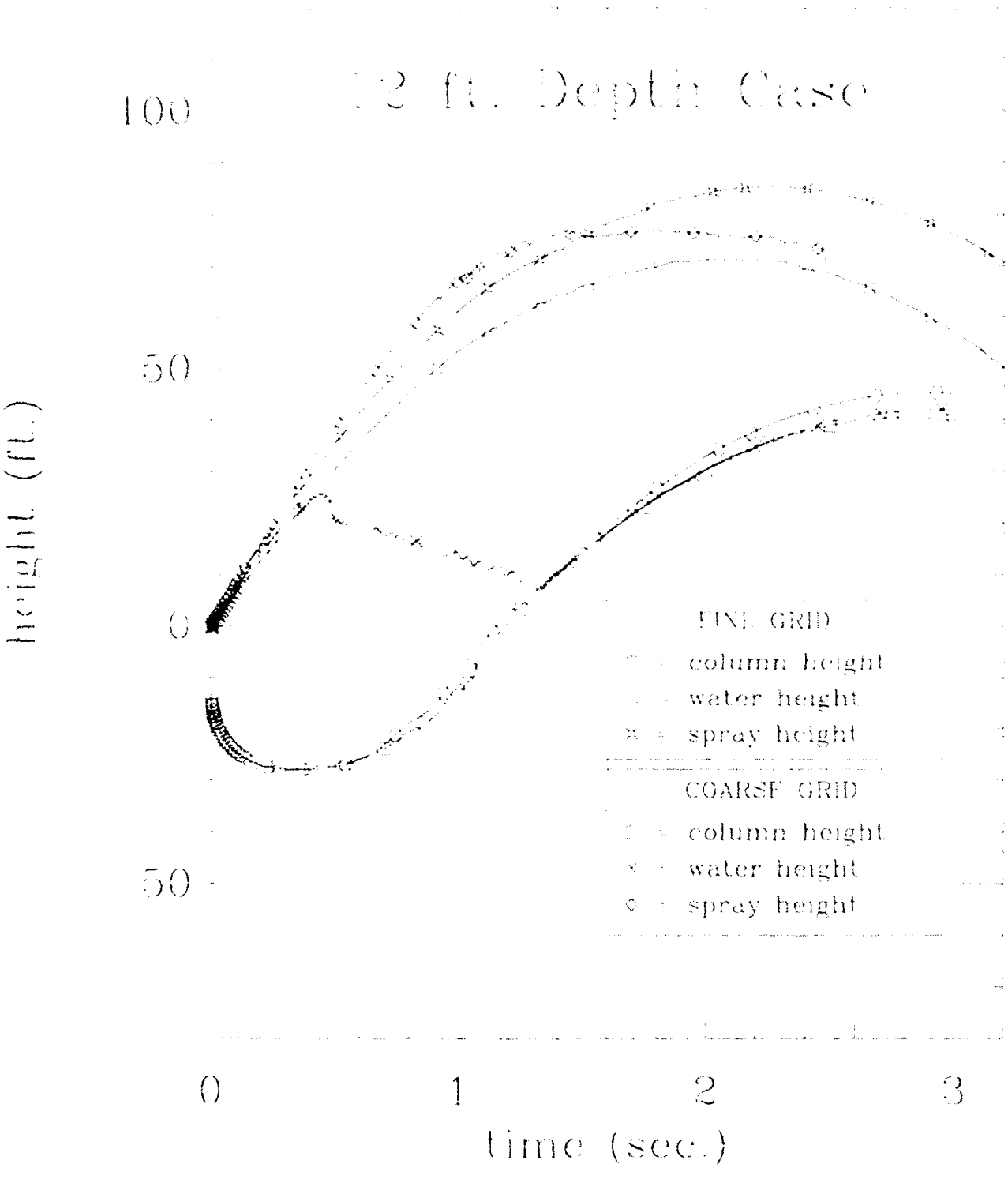

FIGURE 3-4. TIME HISTORIES OF THE MAXIMUM WATER AND SPRAY HEIGHTS FOR THE TWELVE-FOOT DEPTH COMPUTATIONS

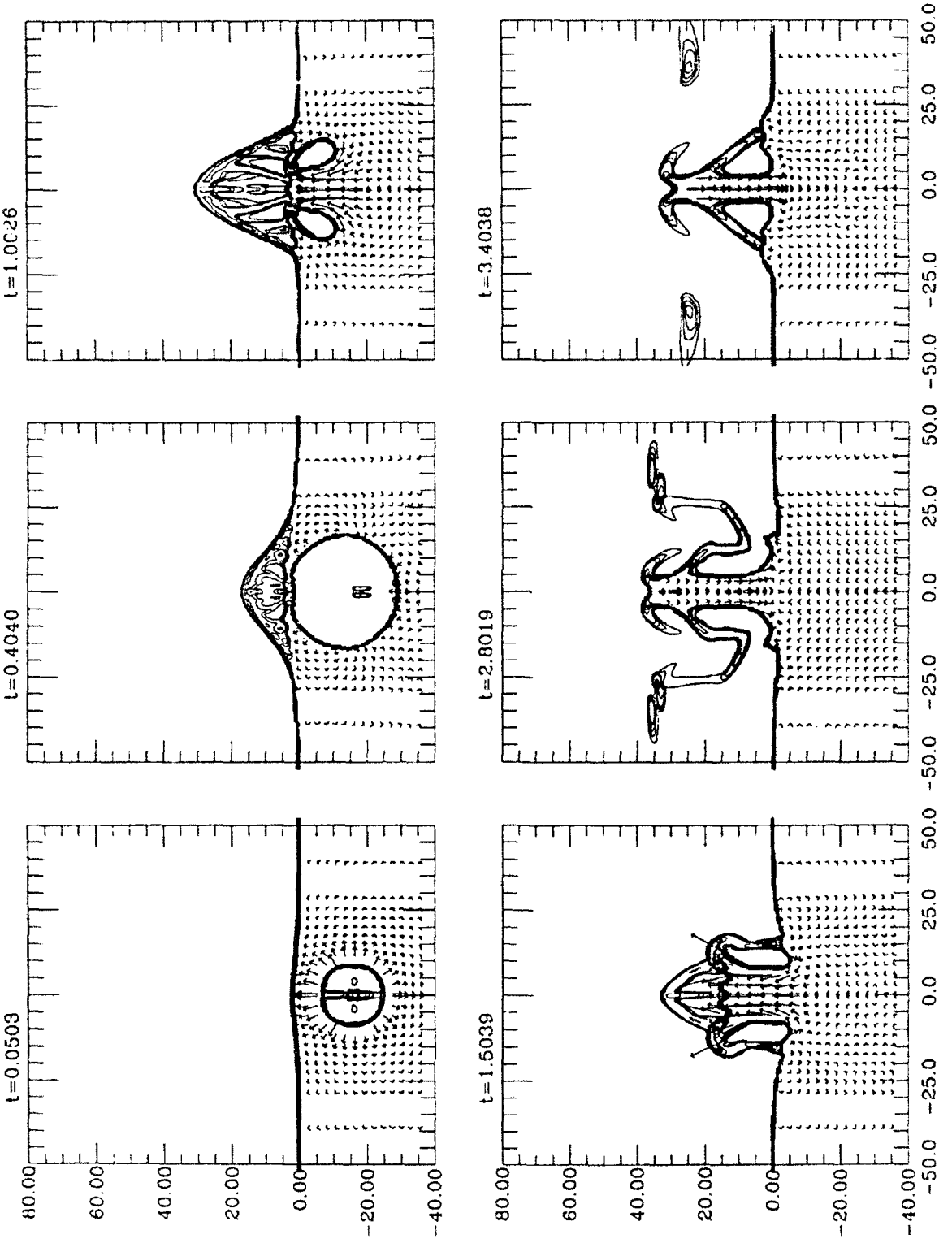

FIGURE 3-5. COARSE GRID INCOMPRESSIBLE COMPUTATION OF A 100-POUND CHARGE OF TNT AT A DEPTH OF SIXTEEN FEET

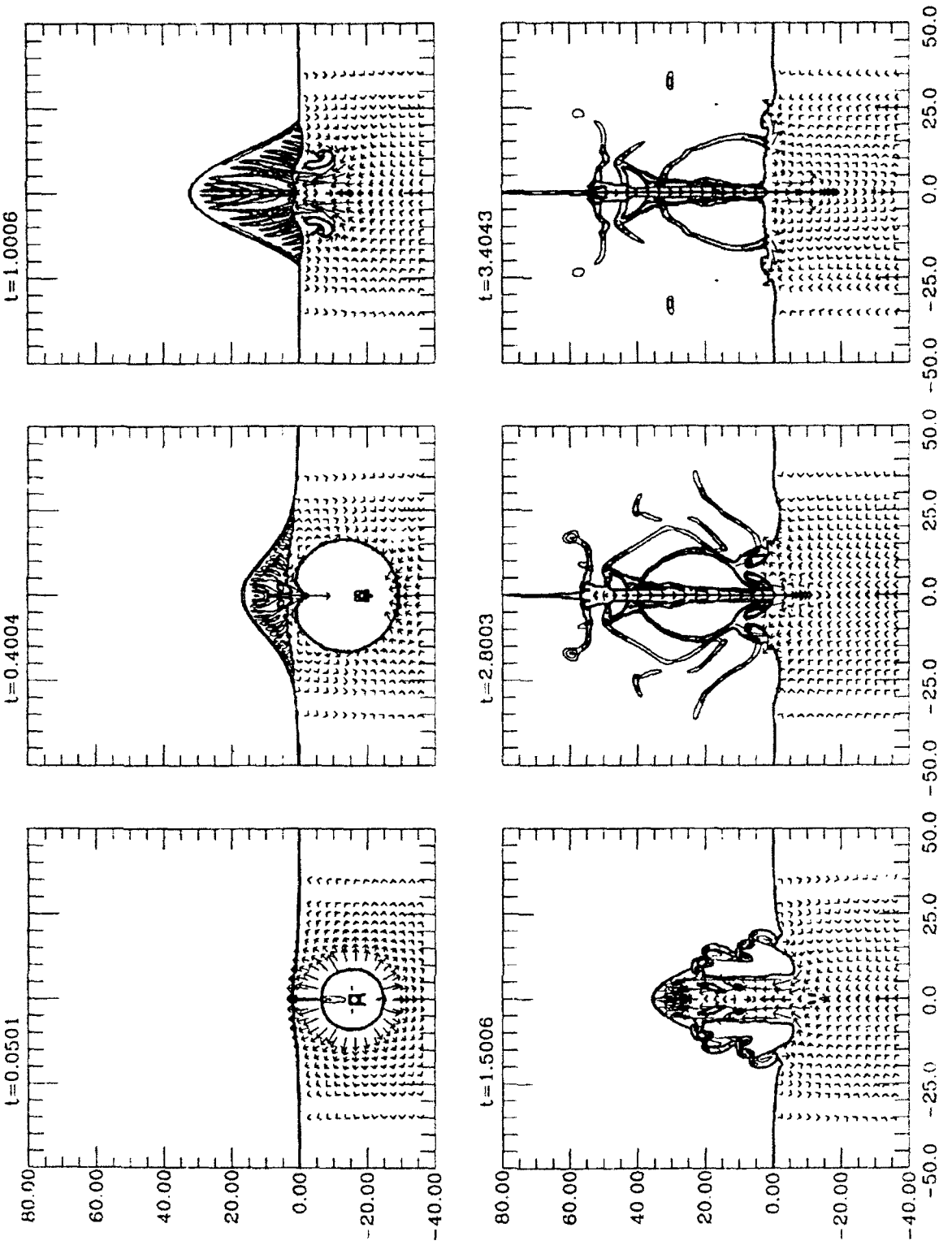

FIGURE 3-6. FINE GRID INCOMPRESSIBLE COMPUTATION OF A 100-POUND CHARGE OF TNT AT A DEPTH OF SIXTEEN FEET

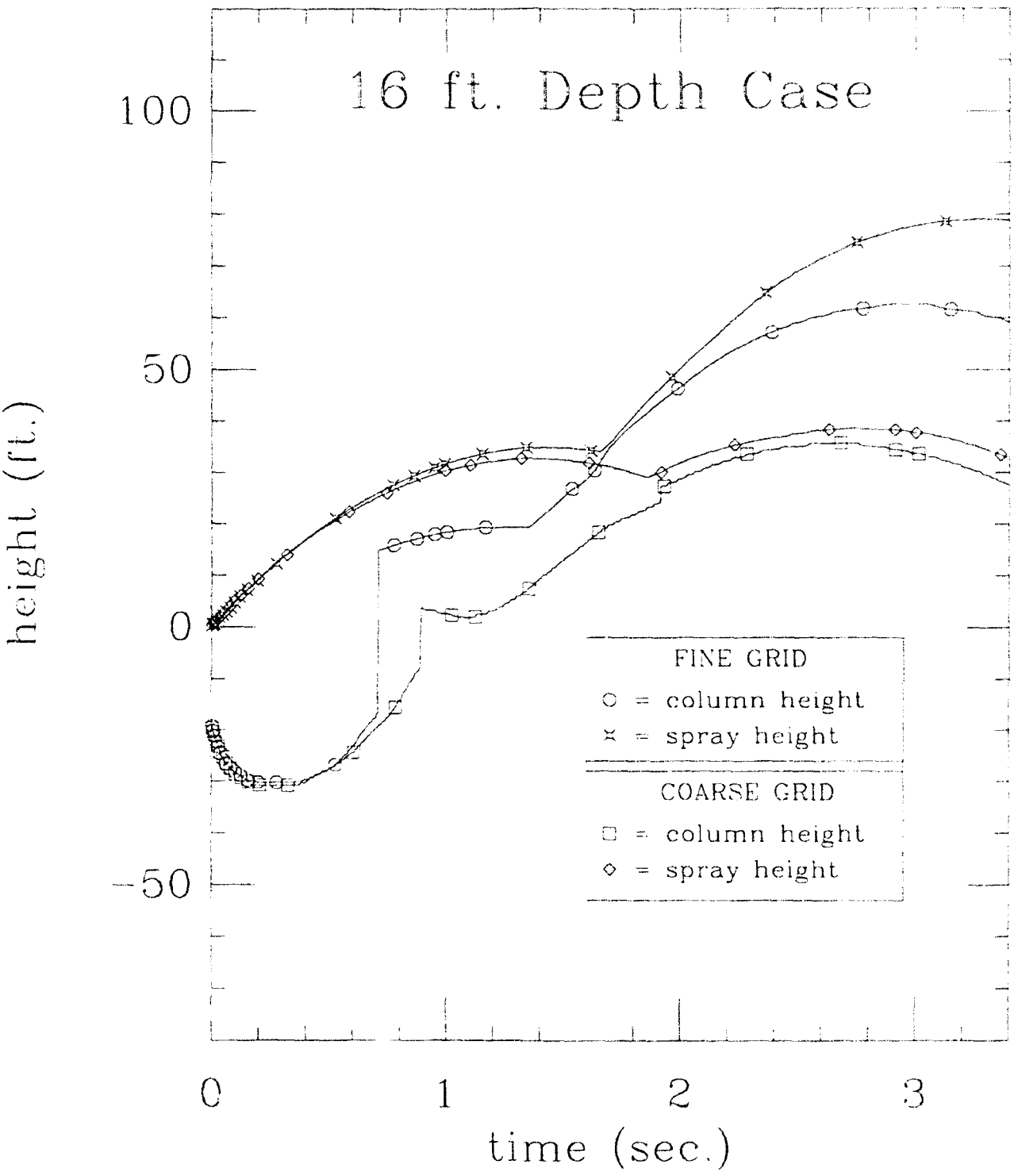

FIGURE 3-7. TIME HISTORIES OF THE MAXIMUM COLUMN AND SPRAY HEIGHTS FOR THE SIXTEEN-FOOT DEPTH COMPUTATIONS

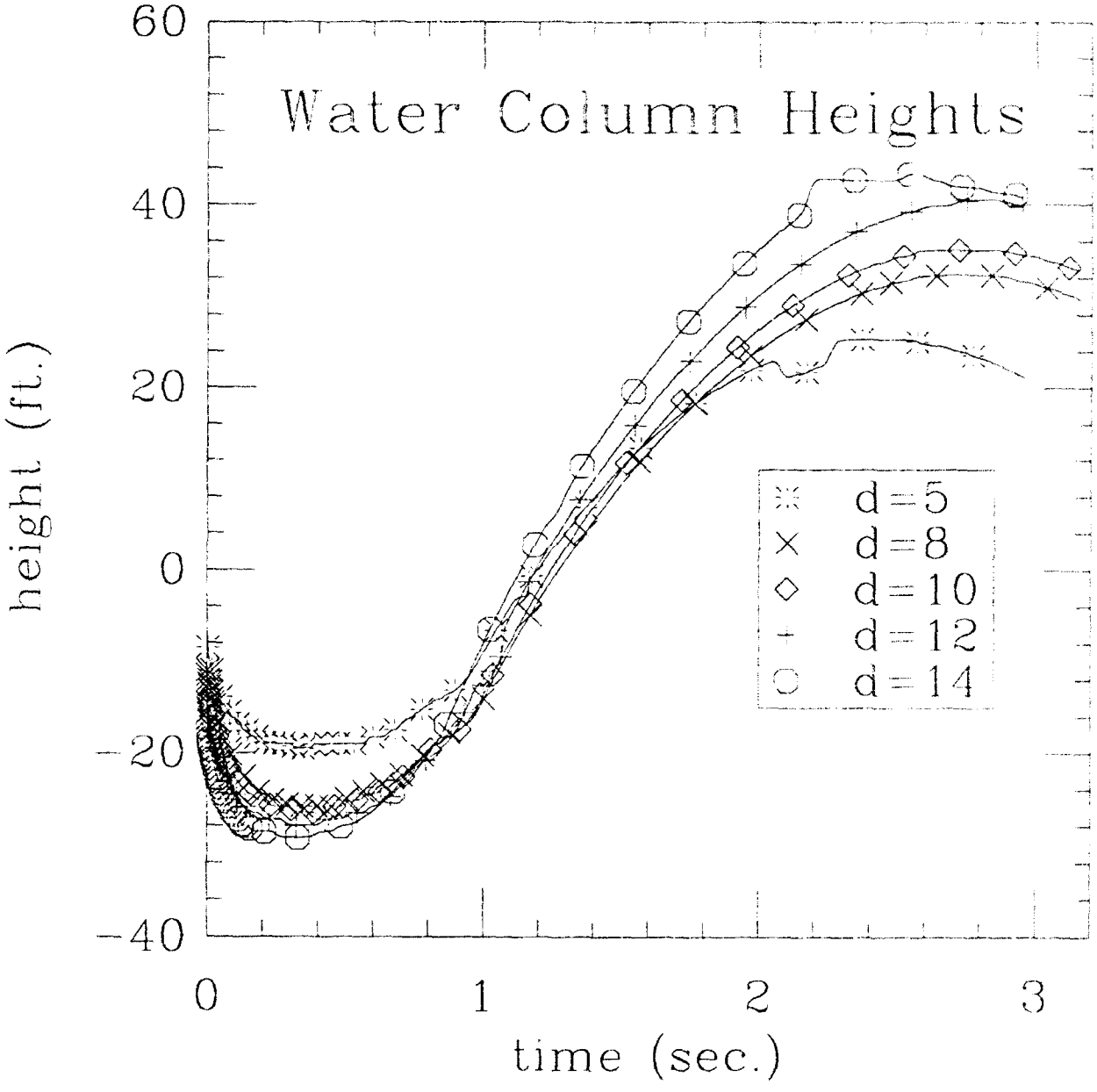

FIGURE 3-8. TIME HISTORIES OF THE MAXIMUM COLUMN HEIGHTS BASED ON THE COARSE GRID COMPUTATIONS AT CHARGE DEPTHS BETWEEN FIVE AND FOURTEEN FEET

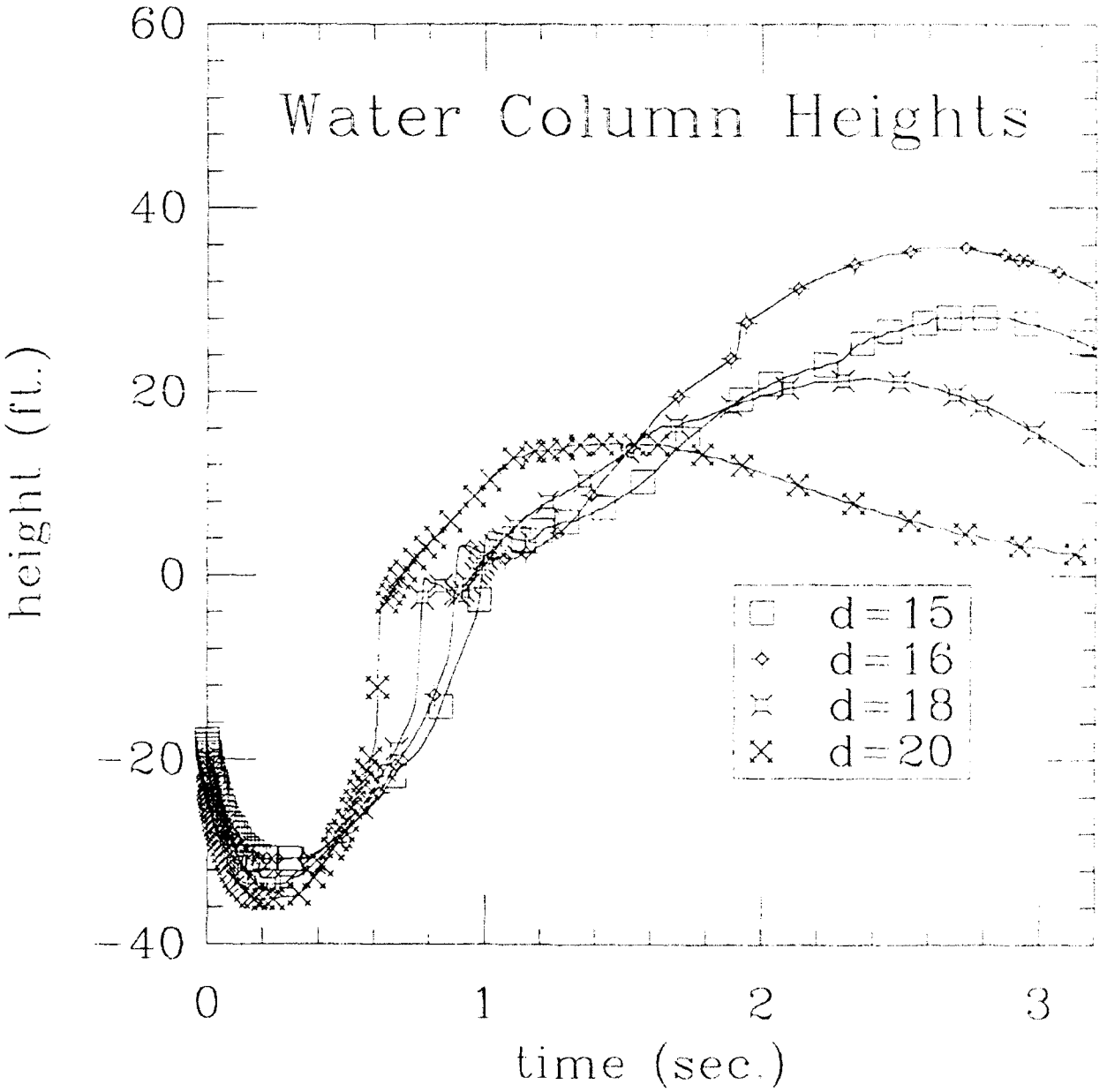

FIGURE 3-9. TIME HISTORIES OF THE MAXIMUM COLUMN HEIGHTS BASED ON THE COARSE GRID COMPUTATIONS AT CHARGE DEPTHS BETWEEN FIFTEEN AND TWENTY FEET

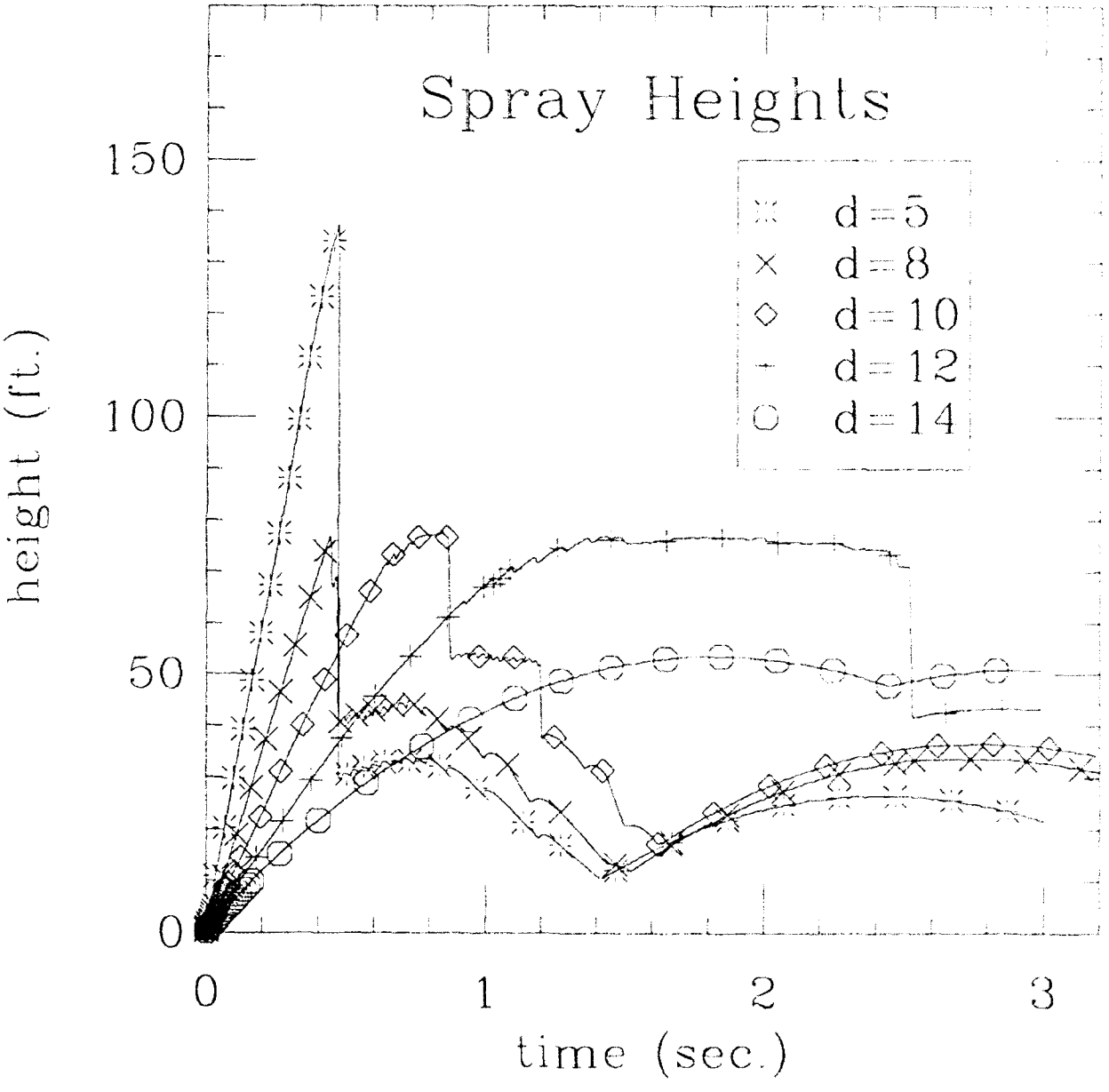

FIGURE 3-10. TIME HISTORIES OF THE MAXIMUM SPRAY HEIGHTS BASED ON THE COARSE GRID COMPUTATIONS AT CHARGE DEPTHS BETWEEN FIVE AND FOURTEEN FEET

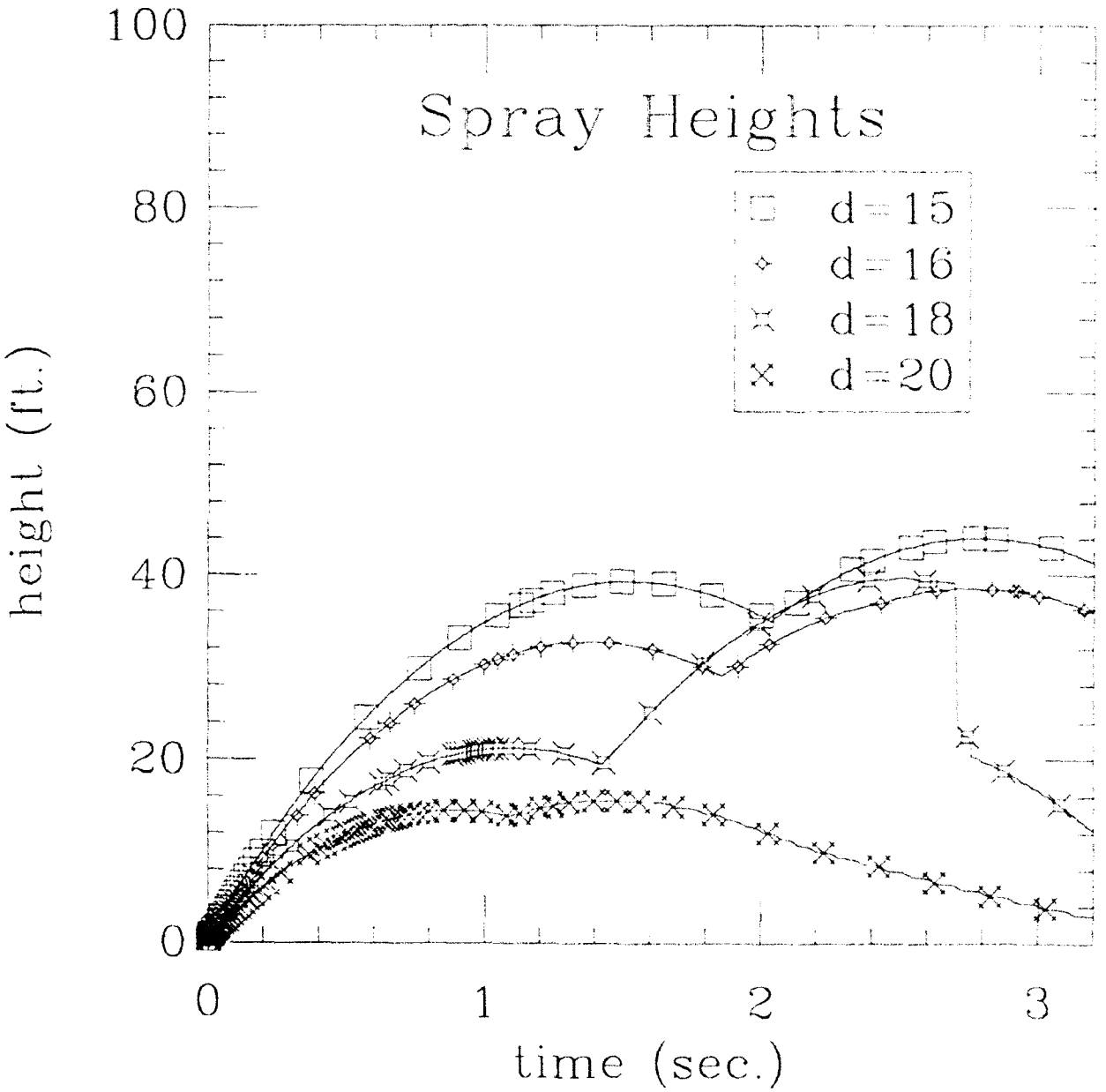

FIGURE 3-11. TIME HISTORIES OF THE MAXIMUM SPRAY HEIGHTS BASED ON THE COARSE GRID COMPUTATIONS AT CHARGE DEPTHS BETWEEN FIFTEEN AND TWENTY FEET

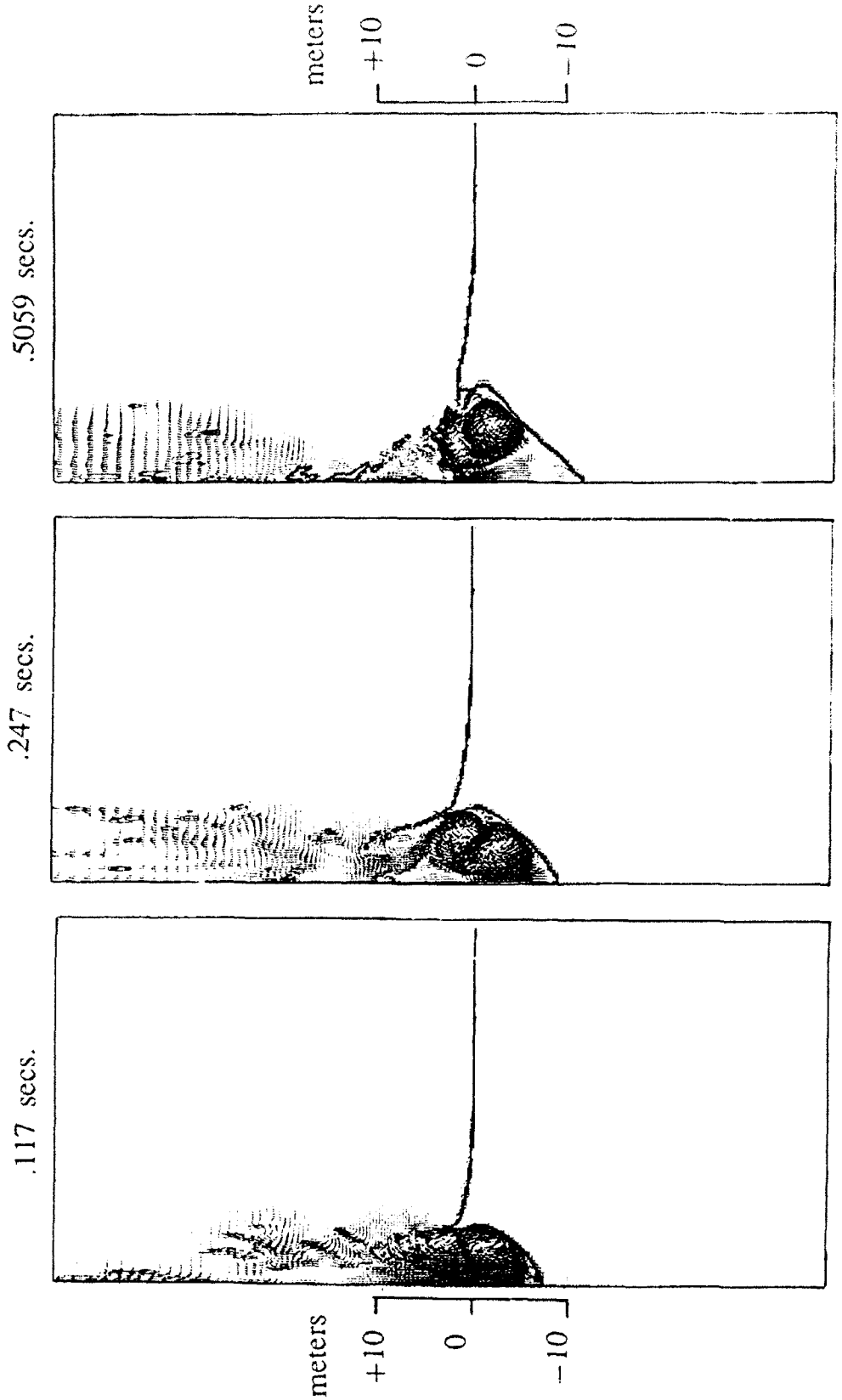

FIGURE 3-12. VELOCITY VECTORS FROM THE COMPRESSIBLE COMPUTATION OF A 300-POUND CHARGE OF TNT AT A DEPTH OF FIVE FEET

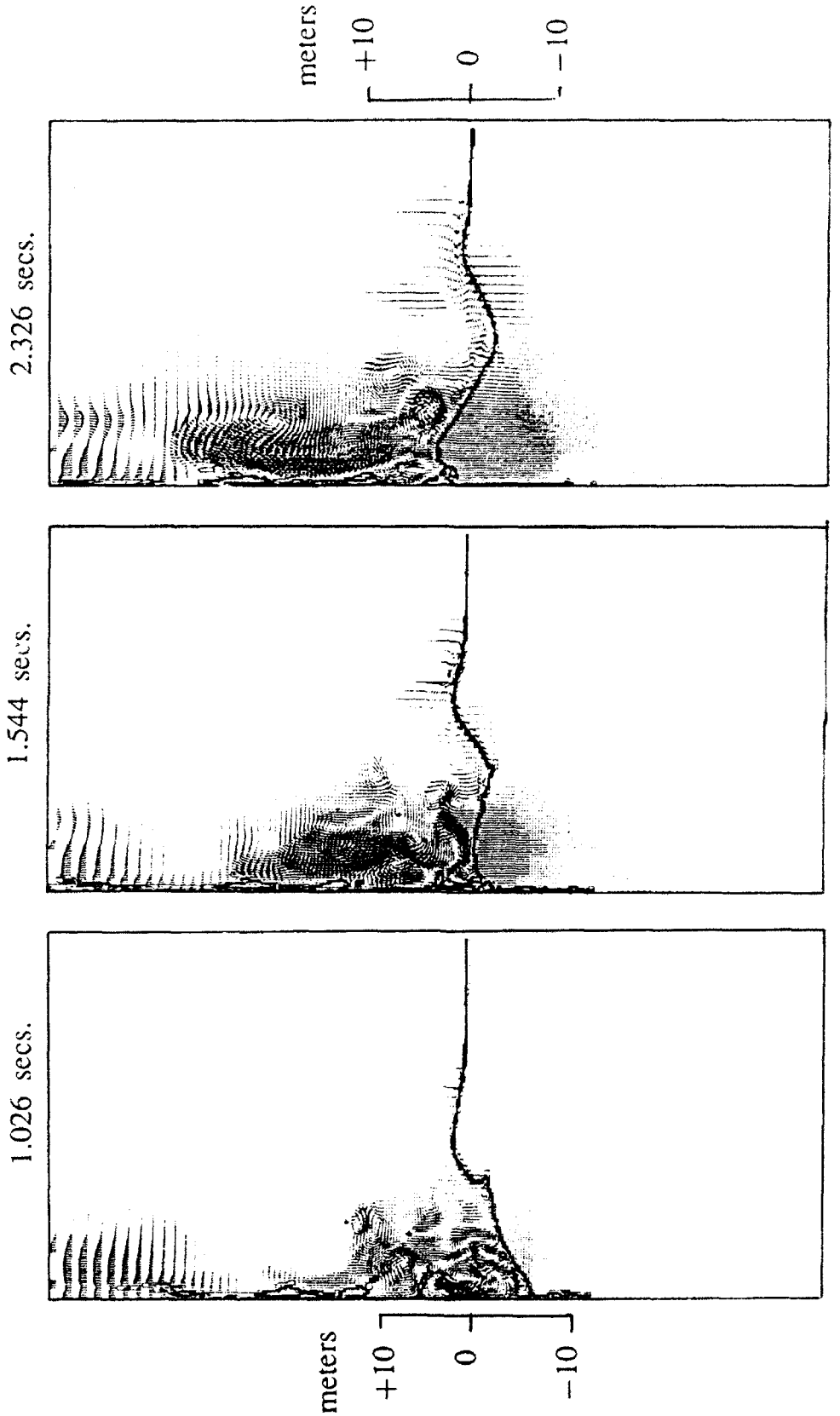

FIGURE 3-12. (CONT.) VELOCITY VECTORS FROM THE COMPRESSIBLE COMPUTATION OF A 300-POUND CHARGE OF TNT AT A DEPTH OF FIVE FEET

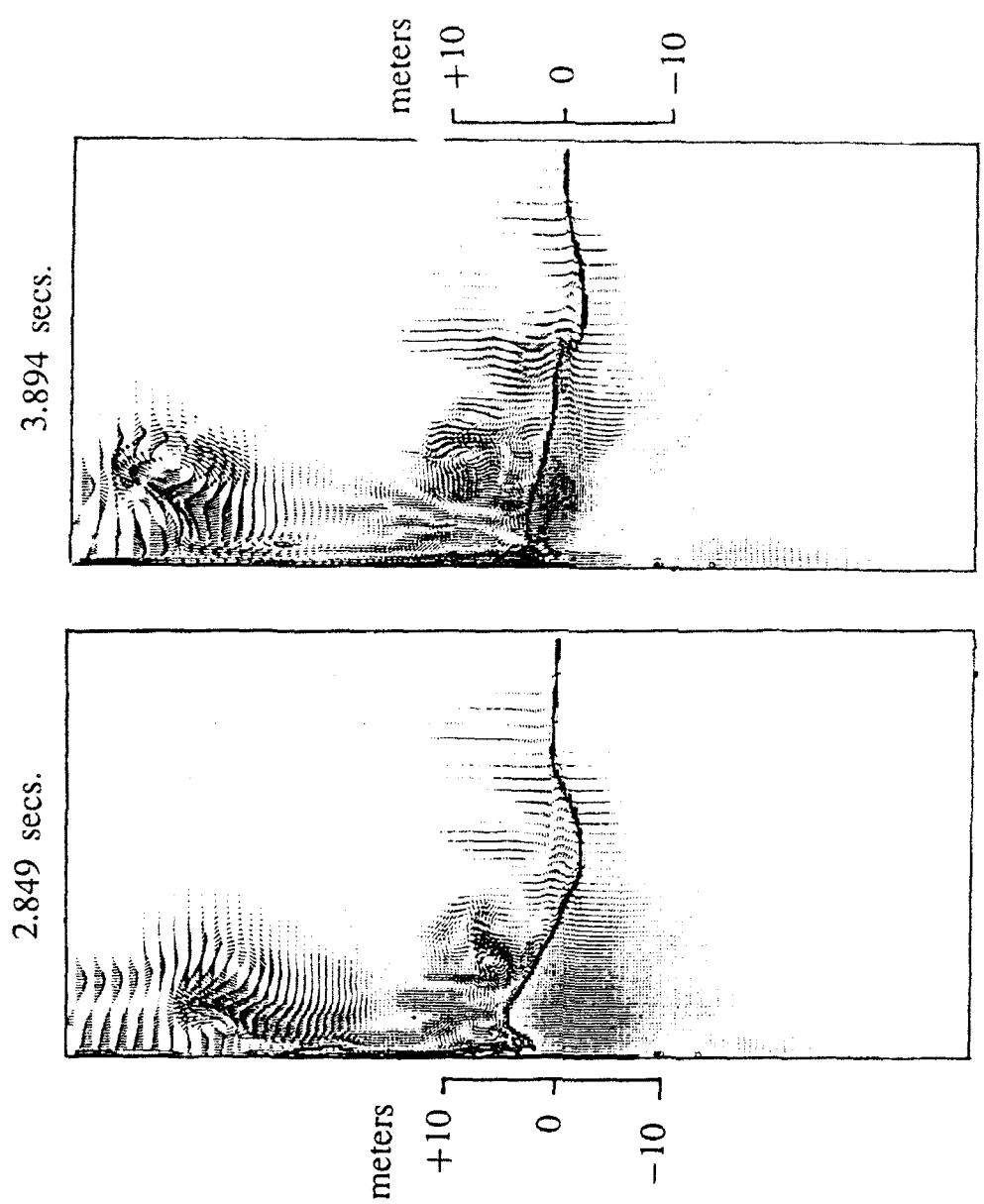

FIGURE 3-12. (CONT.) VELOCITY VECTORS FROM THE COMPRESSIBLE COMPUTATION OF A 300-POUND CHARGE OF TNT AT A DEPTH OF FIVE FEET

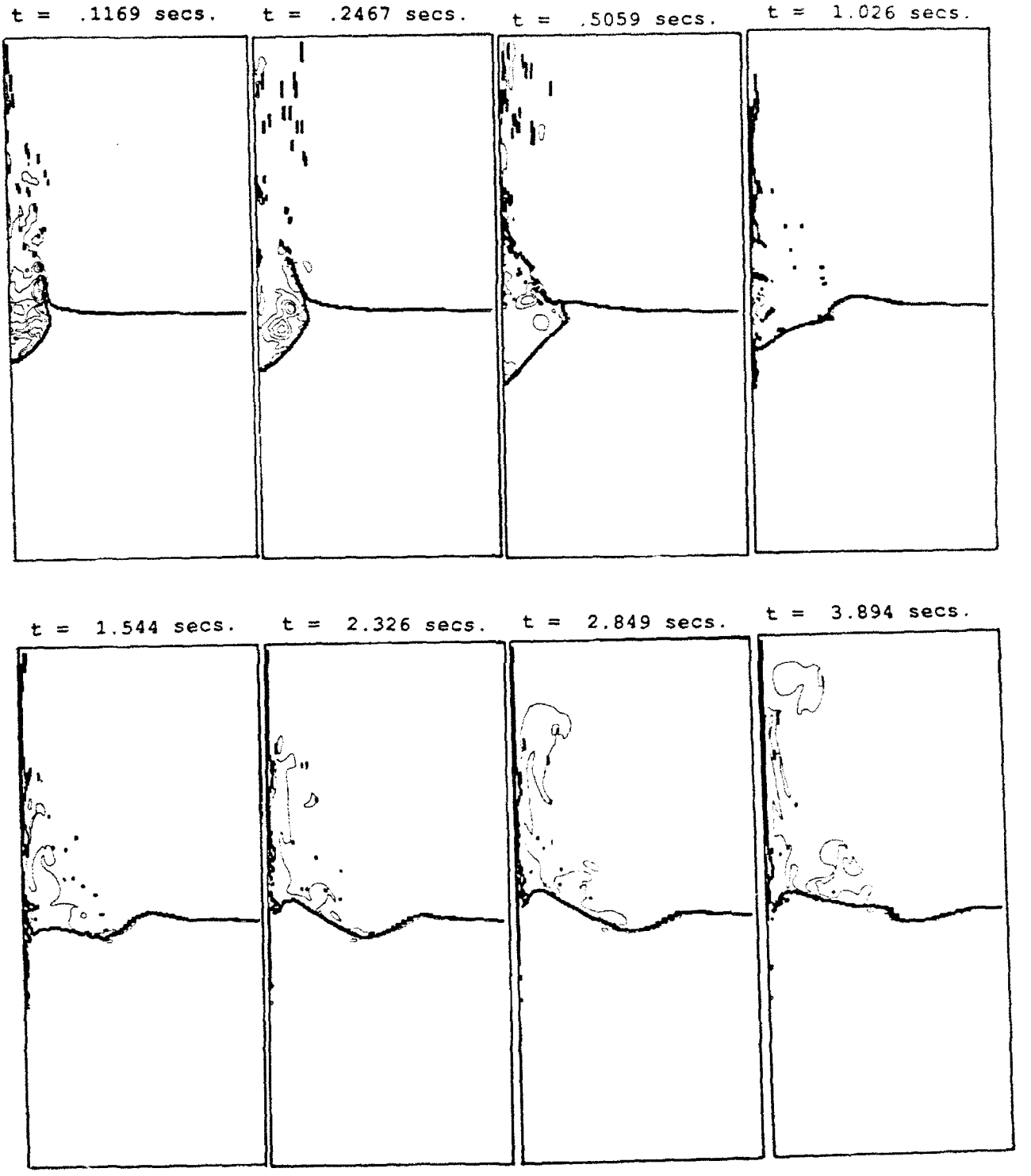

FIGURE 3-13. DENSITY CONTOURS FROM THE COMPRESSIBLE COMPUTATION OF A 300-POUND CHARGE OF TNT AT A DEPTH OF FIVE FEET

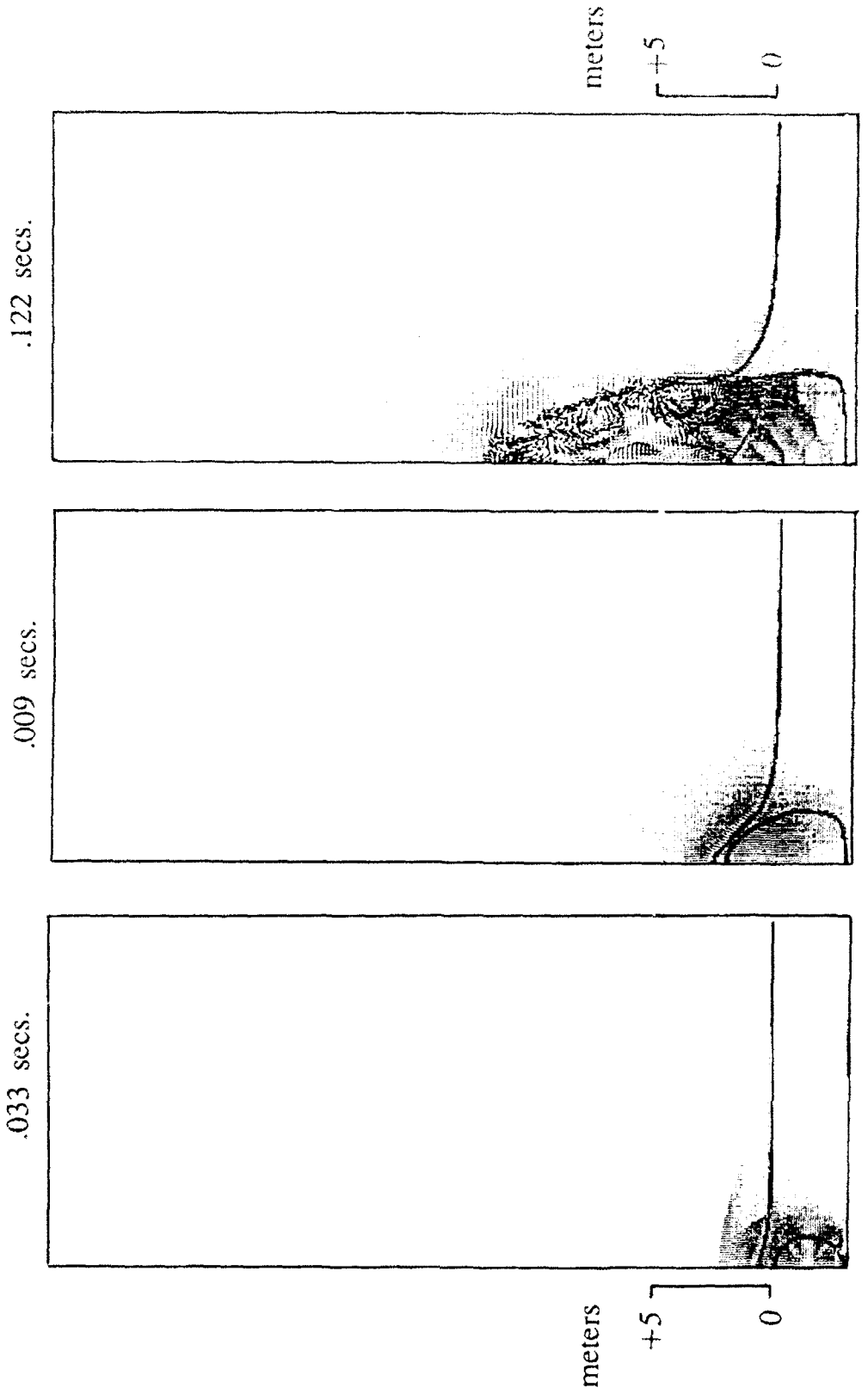

FIGURE 3-14. VELOCITY VECTORS FROM THE COMPRESSIBLE COMPUTATION OF A 100-POUND CHARGE OF TNT IN SHALLOW WATER AT A DEPTH OF 6.5 FEET

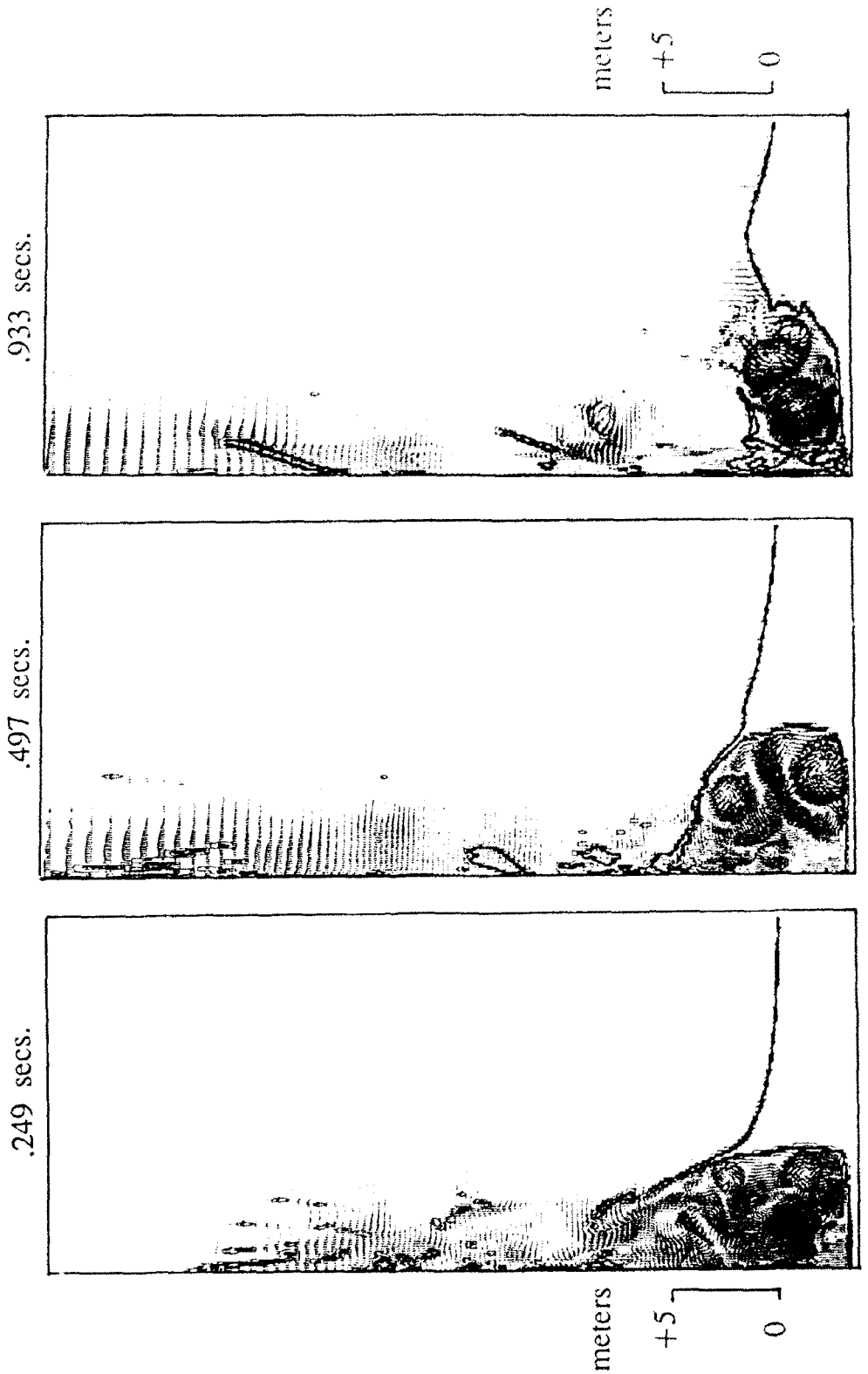

FIGURE 3-14. (CONT.) VELOCITY VECTORS FROM THE COMPRESSIBLE COMPUTATION OF A 100-POUND CHARGE OF TNT IN SHALLOW WATER AT A DEPTH OF 6.5 FEET

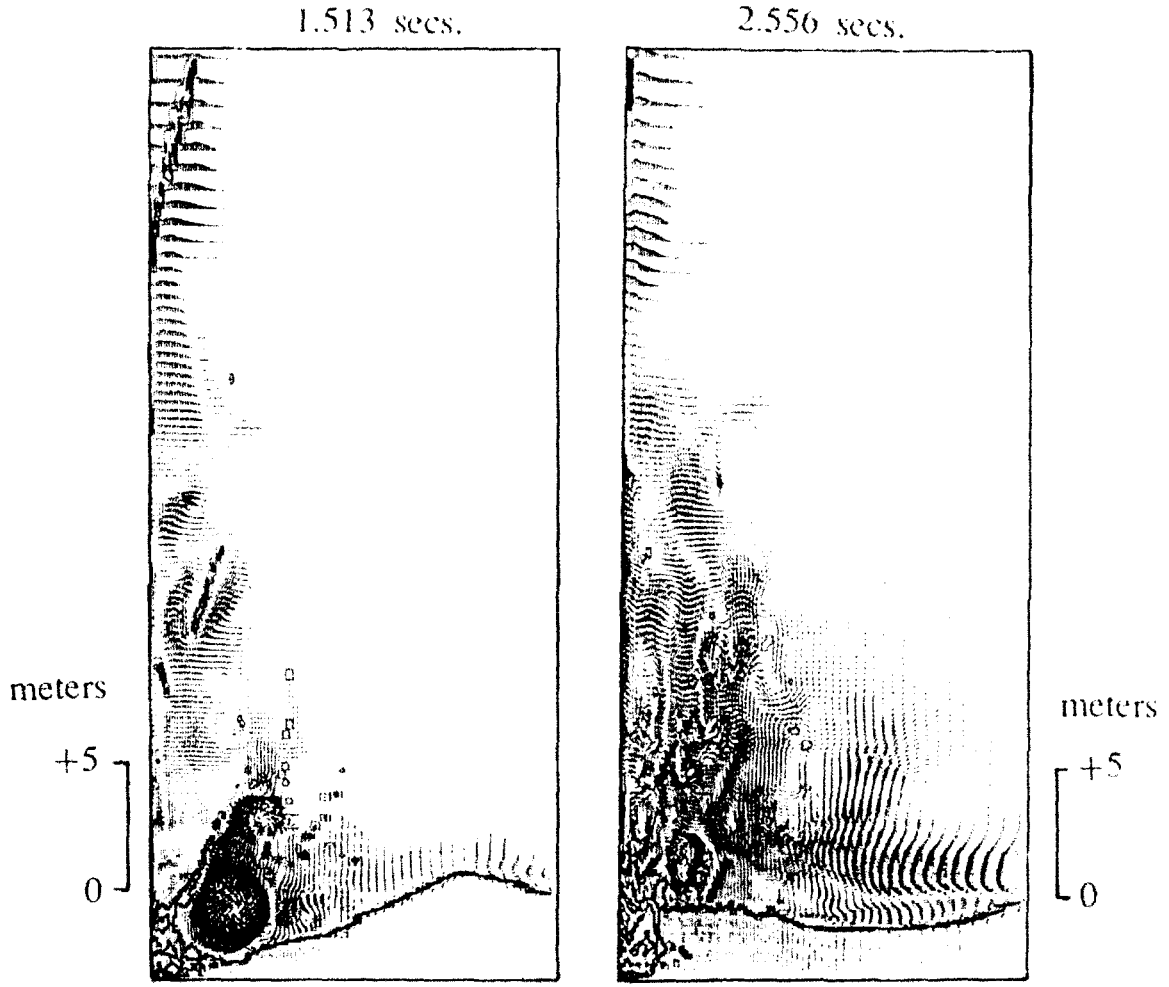

FIGURE 3-14. (CONT.) VELOCITY VECTORS FROM THE COMPRESSIBLE COMPUTATION OF A 100-POUND CHARGE OF TNT IN SHALLOW WATER AT A DEPTH OF 6.5 FEET

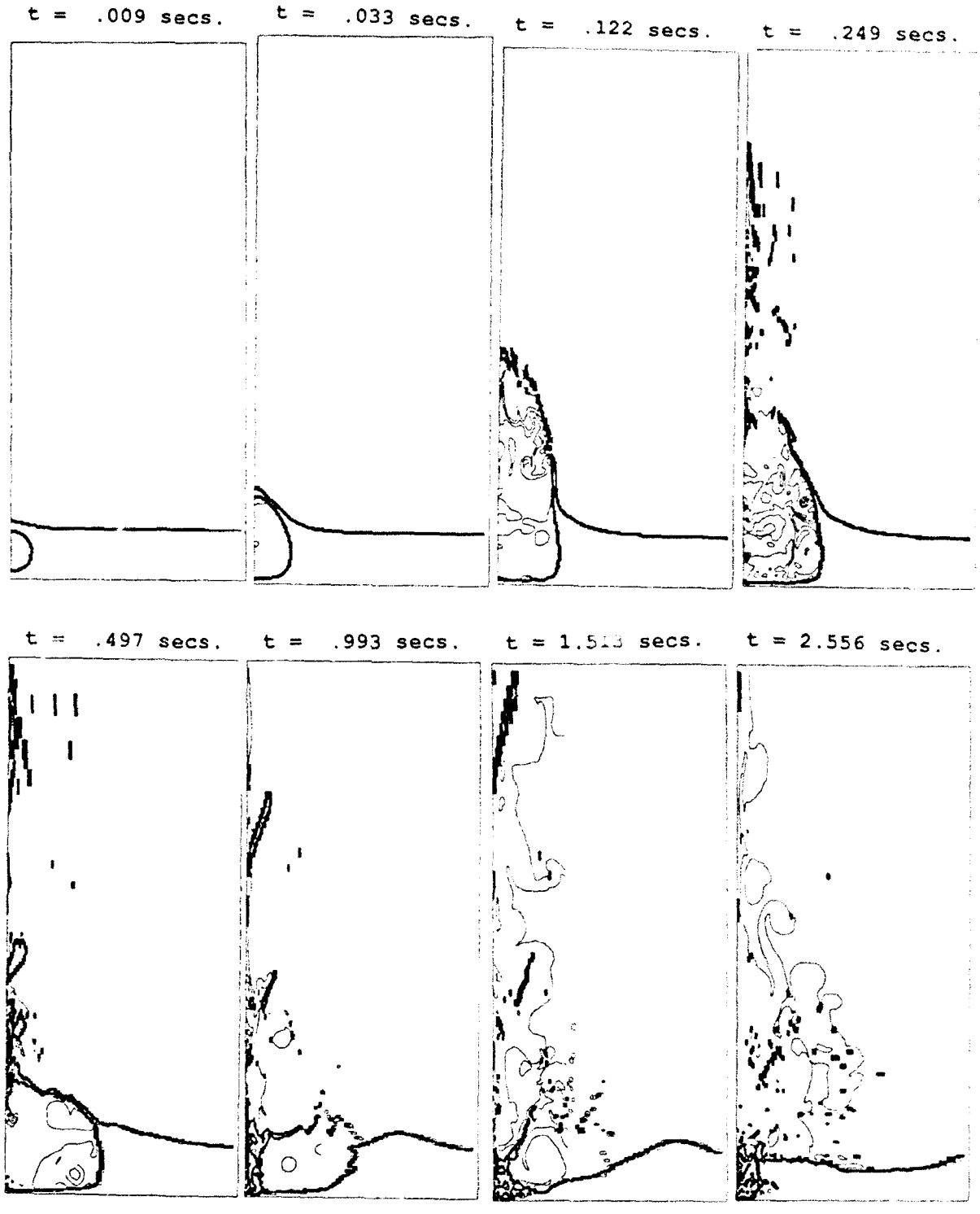

FIGURE 3-15. DENSITY CONTOURS FROM THE COMPRESSIBLE COMPUTATION OF A 100-POUND CHARGE OF TNT IN SHALLOW WATER AT A DEPTH OF 6.5 FEET

CHAPTER 4

CONCLUSIONS

In this paper two different methods were described and used to predict the dynamics of shallow depth explosion plumes. The incompressible code has the advantage of computational efficiency primarily because it selects time steps based on the velocity of the water rather than its much larger sound speed. This code also has the advantage of being validated on predicting underwater bubble dynamics at greater depths.[7,8,9] The compressible code has the advantage of a better physical model in which the effects of the initial shock and the subsequent interaction of air and water can be predicted.

At early times after a shallow depth underwater explosion, the water above the bubble is pushed radially outward, forming a thin water dome rising above the initial water level. A critical event which may occur during this time is the venting of the bubble through the thin water dome into the atmosphere. Both the incompressible and compressible code calculations presented in this report predict that the bubble vents into the atmosphere before the occurrence of the first maximum bubble volume. The venting of the bubble will be predicted numerically by the incompressible code whenever the density of a cell containing the thin dome falls below $(1-\varepsilon_\rho)\rho_0$ (see (2-2)). Thus, the numerical prediction of venting is a function of both the grid size and the value ε_ρ used to determine the cutoff between the liquid and nonliquid cells. Preliminary numerical studies have shown that the selection of ε_ρ can effect the prediction of venting, and have a great effect on the subsequent dynamics of the bubble, cavity and plume. These preliminary computations are in better agreement with the experimental results of Blake and Gibson,[14] which show that spark generated bubbles will not vent at values of $c>0.56$. Shallow depth explosion bubbles which do not vent form a thin water jet above the dome instead of the large cavity which opens up for a venting bubble. The incompressible simulations presented here predict venting at early times for values of c as large as 1. Because of this, the reliability of the calculations could be greatly enhanced by empirically selecting appropriate values for ε_ρ for the incompressible code to better match the predictions of venting. Subsequent research in developing improved predictive capabilities will be focused on this aspect of the calculations.

REFERENCES

1. Cole, R. H., Underwater Explosions, Princeton University Press, Princeton, NJ, 1948.
2. Young, G. A., *Plume and Ejecta Hazards from Underwater Explosions,* NOLTR 73-111, Dec 1973, Naval Surface Warfare Center, Silver Spring, MD
3. Young, G. A., *Dispersions of Chemical Products of Underwater Explosions,* NSWC TR 82-404, Dec 1984, Naval Surface Warfare Center, Silver Spring, MD
4. Higdon, C., *Water Plume Concept for Ship Self Defense,* NAVSWC TR 91-710, 1992, Naval Surface Warfare Center, Silver Spring, MD
5. Colella, P., Glaz, H. M., and Ferguson, R. E., "Multifluid Algorithms for Eulerian Finite Difference Methods," in preparation.
6. Noh, and Woodward, P. R., "SLIC (Simple Line Interface Condition)" UCRL-77651, Aug 1976, Lawrence Livermore National Laboratory, Livermore, CA.
7. Rogers, J. C. W., Szymczak, W. G., Berger, A. E., and Solomon, J. M., "Numerical Solution of Hydrodynamic Free Boundary Problems," in Free Boundary Problems, *Proceedings of the Conference on Free Boundary Problems-Numerical Methods and Optimal Control,* Oberwolfach, Germany, 9-19 July 1989, *Int. Series of Numer. Math.,* Vol. 95., K.-H. Hoffman and J. Sprekels, eds., Birkhaüser Verlag Basel, 1990, pp. 241-266.
8. Szymczak, W. G., Rogers, J. C. W., Solomon, J. M., and Berger, A. E., "A Numerical Algorithm for Hydrodynamic Free Boundary Problems," to appear in *J. Comput. Phys.*
9. Szymczak, W. G., Solomon, J. M., Berger, A. E., and Rogers, J. C. W., "A Numerical Method Based on a Generalized Formulation of Hydrodynamic Free Surface Problems," paper no. AIAA-91-1541-CP, in *Proceedings of the AIAA 10th Computational Fluid Dynamics Conference,* Honolulu, Hawaii, 24-27 June 1991.
10. Rogers, J. C. W., "Incompressible Flows as a System of Conservation Laws with a Constraint," *Seminaires IRIA Analyse et Contrôle de Systèmes* 1978, pp. 141-162.
11. Rogers, J. C. W., "Stability, Energy Conservation, and Turbulence for Water Waves," *Seminaires IRIA Analyse et Contrôle de Systèmes* 1978, pp. 162-180.
12. Colella, P., "A Direct Eulerian MUSCL Scheme for Gas Dynamics," *SIAM J. Sci. Stat. Comput.,* Vol. 6, 1985, pp. 104-117.
13. Snay, H. G., Goertner, J. F., and Price, R. S., *Small Scale Experiments to Determine Migration of Explosion Gas Globes Towards Submarines,* NAVORD report 2280, July 1952.
14. Blake, J. R., and Gibson, D. C., "Cavitation Bubbles Near Boundaries," *Ann. Rev. Fluid Mech.,* Vol. 19, 1987, pp. 99-123.

15. Blake, J. R., Taib, B. B., and Doherty, G., "Transient Cavities Near Boundaries: Part 2. Free Surface," *J. Fluid Mech.*, Vol. 181, 1987, pp. 197-212.

16. Kipp, M. E., Lawrence, M. E., *A One Dimensional Finite Difference Wave Propogation Code*, SAND81-0930, June 1982, Sandia National Laboratory, Albuquerque, NM and Livermore, CA.

DISTRIBUTION

	Copies
Office of Naval Research Attn: Dr. Richard Lau (Code 411) 800 North Quincy Street Arlington, VA 22217	1
Lawrence Livermore National Laboratory Attn: Dr. John Bell Livermore, CA 94550	1
University of Maryland Attn: Dr. S. Antman Department of Mathematics College Park, MD 20742	1
University of Maryland Attn: Dr. I. Babuska	1
Dr. R. B. Kellogg	1
Dr. R. H. Nochetto	1
Institute for Physical Science and Technology College Park, MD 20742	
Defense Technical Information Center Cameron Station Alexandria, VA 22304-6145	12
Attn: Gift and Exchange Division Library of Congress Washington, DC 20540	4
Center for Naval Analyses 4401 Ford Ave. Alexandria, VA 22302-0268	1

Internal Distribution:	Copies
D4 (M. Lacey)	1
E231	2
E232	3
N742 (GIDEP)	1
G05 (T. H. McCants Jr.)	1
G42 (C. E. Higdon)	1
R	1
R04	1
R10A (C. Dickenson)	1
R14 (W. W. McDonald)	1
R14 (G. S. Harris)	1
R14 (G. A. Young)	1
R40	1
R44 (T.-F. Zien)	1
R44 (A. E. Berger)	1
R44 (J. P. Collins)	1
R44 (R. E. Ferguson)	1
R44 (K.-Y. Chien)	1
R44 (A. B. Wardlaw)	15
R44 (F. J. Priolo)	1
R44 (W. G. Szymczak)	15
R44 (J. M. Solomon)	1
G92 (W. A. Walker)	1
G92 (C. W. Smith)	1

REPORT DOCUMENTATION PAGE

Form Approved
OMB No 0704 0188

1. AGENCY USE ONLY (Leave blank)	2. REPORT DATE	3. REPORT TYPE AND DATES COVERED
	12 March 1993	

4. TITLE AND SUBTITLE

Numerical Methods for Explosion Plume Predictions

5. FUNDING NUMBERS

6. AUTHOR(S)

W. G. Szymczak and A. B. Wardlaw

7. PERFORMING ORGANIZATION NAME(S) AND ADDRESS(ES)

Naval Surface Warfare Center
10901 New Hampshire Avenue
Silver Spring, MD 20903-5640

8. PERFORMING ORGANIZATION REPORT NUMBER

9. SPONSORING/MONITORING AGENCY NAME(S) AND ADDRESS(ES)

10. SPONSORING/MONITORING AGENCY REPORT NUMBER

11. SUPPLEMENTARY NOTES

12a. DISTRIBUTION/AVAILABILITY STATEMENT

Approved for public release, distribution is unlimited.

12b. DISTRIBUTION CODE

13. ABSTRACT *(Maximum 200 words)*

A computational study has been conducted of the plume created by an underwater explosion. Calculations have been performed with a compressible and an incompressible method. The later method was found to be more economical in treating the relatively long-term phenomena associated with the explosion plume, which takes several seconds to form and decay. Both techniques suggest that the formation of an explosion plume can be divided into five different phases: cavity formation, cavity collapse, venting, jetting, and rebound. Unfortunately, the internal plume structure predicted by calculation cannot be verified at this time due to the absence of experimental data describing the density distribution within the plume.

14. SUBJECT TERMS

Underwater explosions Explosion plumes

15. NUMBER OF PAGES

49

16. PRICE CODE

17. SECURITY CLASSIFICATION OF REPORT	18. SECURITY CLASSIFICATION OF THIS PAGE	19. SECURITY CLASSIFICATION OF ABSTRACT	20. LIMITATION OF ABSTRACT
UNCLASSIFIED	UNCLASSIFIED	UNCLASSIFIED	SAR